Global chlorophyll a concentrations of phytoplankton functional types with detailed uncertainty assessment using multi-sensor ocean color and sea surface temperature satellite products

Hongyan Xi[1,1], Svetlana Loza (Losa)[1], Antoine Mangin[2], Philippe Garnesson[2], Marine Bretagnon[2], Julien Demaria[2], Marinana A. Soppa[1], Odile Hembise Fanton d'Andon[2], and Astrid Bracher[3]

[1]Alfred Wegener Institute Helmholtz Centre for Polar and Marine Research
[2]ACRI-ST
[3]Alfred-Wegener-Institut für Polar und Meeresforschung,Universität Bremen,Universität Bremen

November 30, 2022

Abstract

Firstly, we re-tune an algorithm based on empirical orthogonal functions (EOF) for globally retrieving the chlorophyll *a* concentration (Chl-a) of phytoplankton functional types (PFTs) from multi-sensor merged ocean color (OC) products. The re-tuned algorithm, namely EOF-SST hybrid algorithm, is improved by: (i) using 30% more matchups between the updated global *in situ* pigment database and satellite remote sensing reflectance (Rrs) products, and (ii) including sea surface temperature (SST) as an additional input parameter. In addition to the Chl-a of the six PFTs (diatoms, haptophytes, dinoflagellates, green algae, prokaryotes and *Prochlorococcus*), the fractions of prokaryotes and *Prochlorococcus* Chl-a to total Chl-a (TChl-a), are also retrieved by the EOF-SST hybrid algorithm. Matchup data are further separated for low and high temperature regimes based on different PFT dependences on SST, to establish the SST-separated hybrid algorithms which further shows improved performance as compared to the EOF-SST hybrid algorithm. The per-pixel uncertainty of the retrieved TChl-a and PFT products is estimated by taking into account the uncertainties from both input data and model parameters through Monte Carlo simulations and analytical error propagation. The uncertainty assessment provided within this study sets the ground to extend the long-term continuous satellite observations of global PFT products by transferring the algorithm and its method to determine uncertainties to similar OC products until today. Satellite PFT uncertainty is also essential to evaluate and improve coupled ecosystem-ocean models which simulate PFTs, and furthermore can be used to directly improve these models via data assimilation.

Global chlorophyll *a* concentrations of phytoplankton functional types with detailed uncertainty assessment using multi-sensor ocean color and sea surface temperature satellite products

Hongyan Xi[1*], Svetlana N. Losa[1,2], Antoine Mangin[3], Philippe Garnesson[3], Marine Bretagnon[3], Julien Demaria[3], Mariana A. Soppa[1], Odile Hembise Fanton d'Andon[3], Astrid Bracher[1,4]

[1] Alfred Wegener Institute, Helmholtz Centre for Polar and Marine Research, Bremerhaven, Germany

[2] Shirshov Institute of Oceanology, Russian Academy of Sciences, Moscow, Russia

[3] ACRI-ST, 06904 Sophia Antipolis Cedex, France

[4] Institute of Environmental Physics, University of Bremen, Bremen, Germany

Correspondence to: H. Xi (Hongyan.Xi@awi.de)

Abstract:

Firstly, we re-tune an algorithm based on empirical orthogonal functions (EOF) for globally retrieving the chlorophyll *a* concentration (Chl-a) of phytoplankton functional types (PFTs) from multi-sensor merged ocean color (OC) products. The re-tuned algorithm, namely EOF-SST hybrid algorithm, is improved by: (i) using 30% more matchups between the updated global *in situ* pigment database and satellite remote sensing reflectance (Rrs) products, and (ii) including sea surface temperature (SST) as an additional input parameter. In addition to the Chl-a of the six PFTs (diatoms, haptophytes, dinoflagellates, green algae, prokaryotes and *Prochlorococcus*), the fractions of prokaryotes and *Prochlorococcus* Chl-a to total Chl-a (TChl-a), are also retrieved by the EOF-SST hybrid algorithm. Matchup data are further separated for low and high temperature regimes based on different PFT dependences on SST, to establish the SST-separated hybrid algorithms which further shows improved performance as compared to the EOF-SST hybrid algorithm. The per-pixel uncertainty of the retrieved TChl-a and PFT products is estimated by taking into account the uncertainties from both input data and model parameters through Monte Carlo simulations and analytical error propagation. The uncertainty assessment provided within this study sets the ground to extend the long-term continuous satellite observations of global PFT products by transferring the algorithm and its method to determine uncertainties to similar OC products until today. Satellite PFT uncertainty is also essential to evaluate and improve coupled ecosystem-ocean models which

simulate PFTs, and furthermore can be used to directly improve these models via data assimilation.

Plain Language Summary:

Phytoplankton in the sunlit layer of the ocean contribute approximately 50% to global primary production. They act as the base of the marine food web fueling fisheries, and also regulate key biogeochemical processes such as exporting carbon to the deep ocean. Phytoplankton contain various taxonomic groups that function differently in the marine ecosystem. The global phytoplankton can be observed from space by analyzing the signal leaving from the water surface recorded by the ocean color sensors onboard the satellites. Based on an updated large global data set, satellite data from different ocean color sensors and sea surface temperature data, we adapted our previous approach to better quantify the biomass of the main six phytoplankton groups on the global scale. The uncertainty of the satellite products of the phytoplankton groups are calculated by considering the errors propagated from the satellite data and the model parameters. This approach for quantifying different phytoplankton groups, together with the uncertainty assessment, can be extended to other similar ocean color satellite data which cover different time periods, to ultimately generate long term global distribution maps of multiple phytoplankton groups. This information will help the modelers to better predict the phytoplankton changes in the future.

Keywords: Algorithm; empirical orthogonal functions; remote sensing reflectance; HPLC pigments; merged products

1 Introduction

Playing a fundamental role in the marine food web and biogeochemical cycling, phytoplankton community structure and taxonomic composition has been widely investigated in the past decades, through various observations methods and ecological modelling (e.g., Falkowski *et al.*, 2003; Le Quéré *et al.* 2005; IOCCG, 2014). With a vast amount of quality-controlled ocean color remote sensing (OC) data, observations of the composition of phytoplankton assemblages have provided various phytoplankton information including dominance of phytoplankton groups, size classes (PSCs) and phytoplankton functional types (PFTs) on a large scale both in space and time. The retrieval algorithms for phytoplankton composition were generally developed based on both *in situ* measurements and satellite products, in which the former provides the ground truth information at specific time and location, but with the latter the continuous spatiotemporal observations can be achieved.

Signals leaving the ocean surface (radiance or reflectance data) recorded by the satellites inherit phytoplankton pigment information that relates to phytoplankton community structure and size classes (Bracher *et al.*, 2017; Mouw *et al.*, 2017). Therefore, they are often used to establish spectral-based approaches to retrieve the concentrations of phytoplankton chlorophyll, pigments and multiple PFTs from space (e.g., Alvain *et al.*, 2005, 2008; Bracher *et al.*, 2009; Werdell *et al.*, 2014; Correa-Ramirez *et al.*, 2018; Xi *et al.*, 2020; Lange *et al.*, 2020). One of the efficient approaches is based on the empirical orthogonal function (EOF) analysis on the spectral Rrs or water leaving radiance. By reducing the high dimensionality of the spectral data, the dominant signals that best describe the variance of the structures lying in the spectra can be assessed to establish the statistical models for predicting ocean color metrics and various phytoplankton pigment and PFT chlorophyll *a* concentrations (Chl-a) (e.g., Lubac and Loisel, 2007; Craig *et al.*, 2012; Taylor *et al.*, 2013; Bracher *et al.*, 2015; Soja-Woźniak *et al.*, 2017; Xi *et al.*, 2020; Lange *et al.*, 2020). Approaches based on EOF analysis also exhibited equivalent skill with little downgrading of the performance when applied to reduced spectral resolution (Bracher *et al.*, 2015), enabling its wide applicability to previous (e.g., SeaWiFS and MODIS) and current (e.g., MODIS, VIIRS and OLCI) multispectral OC sensors and their merged products). In addition, as these approaches are usually trained to retrieve ocean color metrics and PFT information directly from the satellite spectral data, in its application no prior knowledge on the phytoplankton biomass or inherent optical properties (IOPs) is required. This makes the implementation of such approaches straightforward and practical for satellite OC products.

The EOF-based approach proposed by Xi *et al.* (2020) has justified to provide reliable Chl-a retrievals of multiple PFTs on the global scale, through inter-comparisons with other satellite derived PFT and PSC products. However, PFT retrievals by Xi *et al.* (2020) showed rather low performance for prokaryotic phytoplankton. Incorporating additionally environmental parameters, which are globally available from satellite measurements, such as optical depth, sea surface temperature, wind stress, and light availability, have shown improvements to several ocean colour PSC retrievals. For instance, Brewin *et al.* (2015) investigated the influence of light in the mixed layer on the parameters of the three-component PSC model (abundance-based model) of Brewin *et al.* (2010), and modified the model to better describe the relationship between phytoplankton size structure and total chlorophyll with varying light conditions. Ward (2015) and Brewin, Ciavatta, *et al.* (2017) both incorporated temperature dependence into the three-component model and improved the model's ability in representing

Chl-a concentrations in all three PSCs using satellite estimates of SST and total Chl-a concentration.

There has been the emerging trend of the combined use of *in situ* data, satellite observations, ecosystem modelling (Losa *et al.* 2019), as well as PFT or PSC data assimilation (Xiao and Friedrichs, 2014; Pradhan *et al.*, 2020), to allow comprehensive monitoring and predictions of phytoplankton community structure. Satellite derived phytoplankton group-specific products are also expected to be useful for validation of ecosystem model results (e.g., Ward *et al.*, 2012; Hirata *et al.*, 2013; Holt *et al.*, 2014; de Mora *et al.*, 2016; Dutkiewicz *et al.* 2015; Pradhan *et al.* 2019). One of the challenges to fulfill these tasks is associating the uncertainty to the satellite derived PFT products (Bracher *et al.*, 2017). Uncertainty estimates have been well formulated and generated for other common OC algorithms that use satellite radiance and reflectance data to derive OC products such as marine Chl-a concentration, diffuse attenuation coefficient, and inherent optical properties (Werdell *et al.*, 2018, McKinna *et al.*, 2019). Though various approaches have been proposed to derive globally satellite phytoplankton group products (Mouw *et al.* 2017), only the study by Brewin, Ciavatta, *et al.* (2017a) has provided estimates of uncertainty on a per-pixel basis for the North Atlantic Ocean. Uncertainty assessment can be carried out via two methods: validation through comparison of the satellite retrievals with *in situ* data (e.g., Antoine *et al.* 2008; Sathyendranath *et al.*, 2019), or error propagation by accounting for the uncertainties in the inputs and model parameters. Due to sparse distribution of the *in situ* measurements that restrict the validation for the uncertainty estimation (Mélin and Franz, 2014), the error propagation analysis has now been widely used to understand the sensitivity of the model inputs and parameters to the outputs, and produce pixel-by-pixel uncertainty (e.g., Maritorena *et al.*, 2010; Lee *et al.*, 2010; Kostadinov *et al.*, 2016; Qi *et al.*, 2017; Brewin, Tilstone, *et al.*, 2017).

In this work, we improve the previously developed EOF-based algorithm of Xi *et al.* (2020) for global retrievals of multiple PFT quantities by 1) including more matchup data between the *in situ* pigment data set and satellite Rrs data from merged OC products, 2) accounting for the sea surface temperature (SST) in the retrieval scheme, and 3) investigating the influence of SST on the model parameters and the retrieved PFTs with the goal of establishing a set of EOF-SST hybrid algorithms and improving the retrievals of TChl-a, Chl-a of six PFTs and the fractions of two prokaryotic phytoplankton. By applying the hybrid algorithms to the merged OC products, we present the global distribution maps of the

retrieved PFT quantities, and present a method to derive the per-pixel uncertainty propagated from both the inputs and retrieval model for each satellite retrieved PFT quantity by combining Monte Carlo (MC) simulations and an analytical approach.

2 Data and Methods

2.1 Data sets

2.1.1 *In situ* data set of phytoplankton pigments

We updated the large global and open ocean (> 200 m) phytoplankton pigment data set (spanning 2002-2012) from Losa *et al.* (2017) used in Xi *et al.* (2020) analyzed by High Performance Liquid Chromatography (HPLC), by adding recently published HPLC pigment data (by February 2020) from SeaBASS, PANGAEA, British Oceanographic Data Centre (BODC), and Open Access to Ocean Data (AODN) from Australia. All collected data were quality controlled following the method by Aiken *et al.* (2009). A total of 9,595 sets of pigment data were obtained as shown in Figure 1 with the distribution of total chlorophyll a concentration (TChl-a). In the database all required pigments for the PFT Chl-a calculation were included (fucoxanthin, peridinin, 19'hexanoyloxy-fucoxanthin, 19'butanoyloxy-fucoxanthin, alloxanthin, total chlorophyll *b*, zeaxanthin and divinyl chlorophyll *a*).

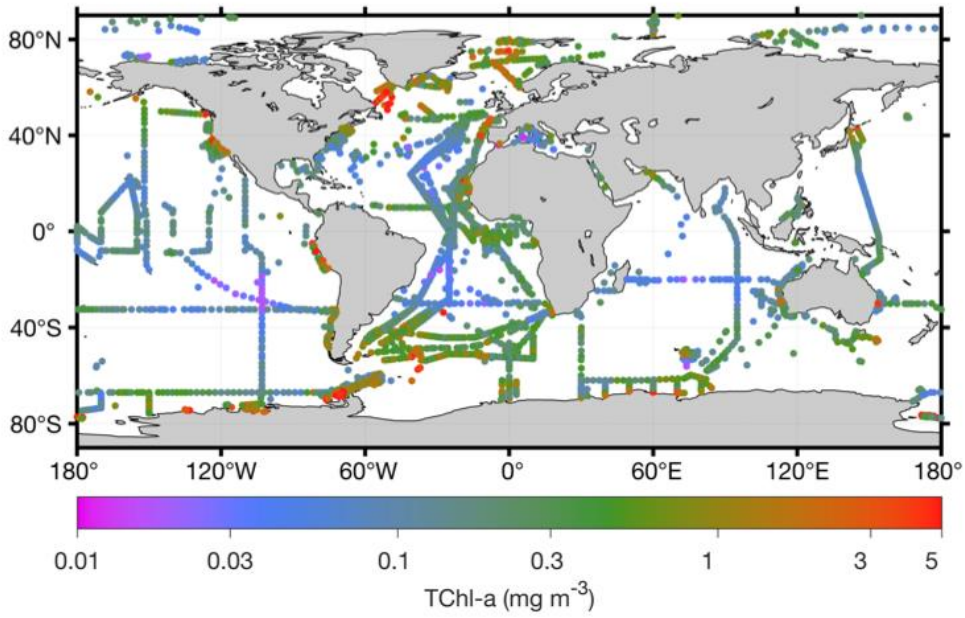

Figure 1. Distribution of TChl-a (the sum of monovinyl chlorophyll *a*, divinyl chlorophyll *a*, chlorophyll *a* allomers, chlorophyll *a* epimers, and chlorophyllide *a*) from the quality controlled *in situ* pigment database (2002 – 2012) used in this study.

2.1.2 Satellite data

2.1.2.1 Satellite ocean color products

GlobColour data archive (http://www.globcolour.info/) has provided various OC products from different sensors, including SeaWiFS, MODIS/AQUA, MERIS, VIIRS onboard Suomi-NPP and Sentinel-3A OLCI. In this study, we used the SeaWiFS-MODIS-MERIS merged normalized remote sensing reflectance (Rrs) Level-3 (L3) product (hereafter referred to as merged product) which covers the period from July 2002 to April 2012 from the GlobColour data archive (http://www.globcolour.info/; more details in ACRI-ST GlobColour Team *et al.*, 2017). As in Xi et al. (2020), the daily merged product with 4-km resolution was used for matchup extraction and monthly merged product with 25-km resolution was used for algorithm application. Since this study focuses mainly on oceanic waters, shelf and coastal waters (< 200 m) were masked out in the OC products using the ETOPO1 bathymetry (Amante and Eakins, 2009).

2.1.2.2 Sea surface temperature (SST) data

The SST product used in this study was CMEMS OSTIA (Operational SST and Ice Analysis) reprocessed analysis product, which is available on the CMEMS (Copernicus Marine Environment Monitoring Service, https://marine.copernicus.eu/) platform, referenced as SST_GLO_SST_L4_REP_OBSERVATIONS_010_011. The CMEMS OSTIA reprocessed analysis product is an interpolated product based on *in situ* measurements and satellite observations from both infra-red and micro-wave data on a global regular grid at 0.05° resolution (Donlon *et al.*, 2012; Worsfold *et al.*, 2020). The SST daily product from July 2002 to April 2012 was acquired and gridded to 4-km resolution. As for Rrs, monthly mean SST product from 2002 to 2012 with 25-km resolution were also processed as input for deriving global satellite PFT products.

2.1.3 Input data for PFT retrieval algorithm

2.1.3.1 *In situ* PFT Chl-a concentration and fraction derived from diagnostic pigment analysis (DPA)

As described in Xi *et al.* (2020), Chl-a of PFTs were derived using an updated DPA method (Soppa *et al.*, 2014; Losa *et al.*, 2017), that was originally developed by Vidussi *et al.*, 2001, adapted in Uitz *et al.* (2006) and further refined by Hirata *et al.* (2011) and Brewin *et al.* (2015). We used pigment concentrations from the *in situ* data base mentioned in Section 2.1.1 to derive the Chl-a of six PFTs – diatoms, dinoflagellates, haptophytes, green algae,

prokaryotes, and *Prochlorococcus*. The partial coefficients of the diagnostic pigments used in the DPA were the updated ones using a large global pigment data set as detailed in Table S1 in Losa *et al.* (2017), which were proved to be in good agreement with previous studies. Due to the weak retrieval performance of prokaryotes and *Prochlorococcus* Chl-a in Xi *et al.* (2020), in this study we included the fractions of prokaryotes (*f*-prokaryotes) and *Prochlorococcus* (*f-Prochlorococcus*) to TChl-a, attempting to get improved retrievals of these two PFTs. PFT Chl-*a* lower than 0.005 mg m^{-3} were excluded due to high uncertainty (Xi *et al.*, 2020) and the corresponding fractions of prokaryotes and *Prochlorococcus* were also excluded.

2.1.3.2 Matchups between satellite SST and *in situ* PFT data

SST matchup data were extracted by matching spatially co-localized and temporally (on a daily basis) coincident with the *in situ* PFT measurements. A macro-pixel of 3×3 pixel centered on the *in situ* measurement was considered. If the standard deviation within this macro-pixel was lower than 25%, then the macro-pixel was considered suitable for the matchup. The median of the macro-pixel is defined as the SST value for the *in situ* site. Though the OSTIA SST product is quality controlled, abnormal values below -2 °C still existed, but were removed in the matchup data.

2.1.3.3 Matchups of Rrs merged product to *in situ* PFT and satellite SST data

Matchups of satellite R_{rs} to *in situ* PFT data (which were also matchups to SST) were extracted from global 4-km daily merged products. The same extraction and averaging protocol including quality control as in Xi *et al.* (2020) were used to derive the single pixel matchups. As justified in Xi *et al.* (2020), due to more matchup points and equivalent retrieval performance compared to 3×3 matchups, the single pixel matchup data set was taken as input data for the final retrieval approach (Figure 2). The Rrs matchup data with the nine bands of 412, 443, 490, 510, 531, 547, 555, 670 and 678 nm from the merged products were chosen as the algorithm input data (Table 1). A total of 508 sets of matchup data covering the global ocean were extracted (Figure 2).

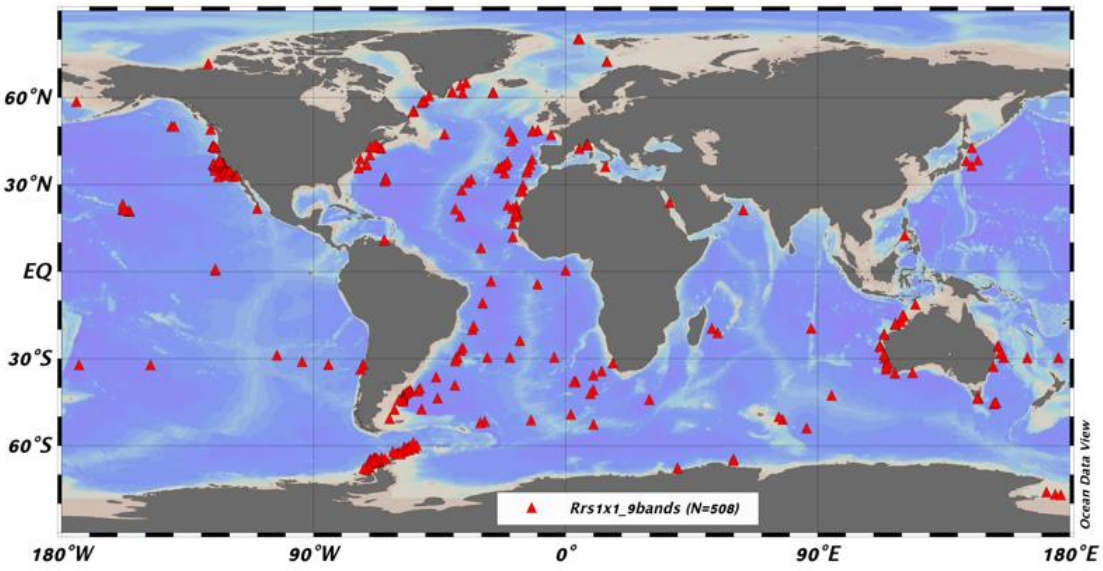

Figure 2. Geographical locations of single pixel matchups of GlobColour merged R_{rs} at nine bands with *in situ* PFT and satellite SST data.

Table 1. List of the nine bands from sensors SeaWiFS, MODIS, and MERIS used in the GlobColour merged products.

Sensors	Center Wavebands (nm)								
	412	443	490	510	531	547	555	670	678
SeaWiFS	×	×	×	×			×	×	
MODIS	×	×	×		×	×	×	×	×
MERIS	×	×	×	×			×*	×	

* There was no band at 555 nm for MERIS itself, but the GlobColour Team provided for MERIS the 555 nm through an inter-spectral conversion made by using:

$R_{rs}(555) = R_{rs}(560) * (1.02542 - 0.03757 * y - 0.00171 * y^2 + 0.0035 * y^3 + 0.00057 * y^4)$, where y = log10(CHL1) and CHL1 is the total Chl-a concentration estimated by OC4 (ACRI-ST GlobColour Team *et al.*, 2017). With this conversion, R_{rs} at 555 nm for MERIS were also included in our study.

2.2 Algorithm re-tuning

The EOF-based PFT retrieval algorithm development and performance assessment were detailed in Xi *et al.* (2020). Using the updated matchup data base, Xi *et al.* (2020) algorithm was re-tuned and statistically assessed as detailed below. Figure 3 shows the scatterplots of the matchup data of SST to TChl-a, the six PFT Chl-a and the two PFT fractions. Generally, TChl-a, diatoms, haptophytes, dinoflagellates, and green algae show decreasing Chl-a with increasing SST. However, Prokaryotes and *Prochlorococcus* Chl-a and their fractions to TChl-a show positive correlation with SST. The statistically significant correlations indicate that introducing SST as an additional term into the Xi *et al.* (2020) algorithm (see Section 2.2.1) might improve the algorithms' performance. Besides, at SST of around 8 °C, with

applying a 10-point running mean to the matchup data, there is a clear shift in the trends of most PFT quantities as a function of SST. This further led us to establish for SST < 8 °C a different EOF-SST hybrid algorithm than for SST ≥ 8 °C (see Section 2.2.2). *Prochlorococcus* data, as an exception from other PFTs, are rarely recorded in high latitudes with low temperature (Flombaum *et al.*, 2013). Our matchup data set contained few (n = 6) divinyl chlorophyll *a* (a marker pigment of *Prochlorococcus*) measurements with low concentrations when SST < 8 °C. To construct the prediction models for all the PFTs more easily, we excluded the regions where SST is below 8 °C for the Chl-a and fraction retrievals of *Prochlorococcus*.

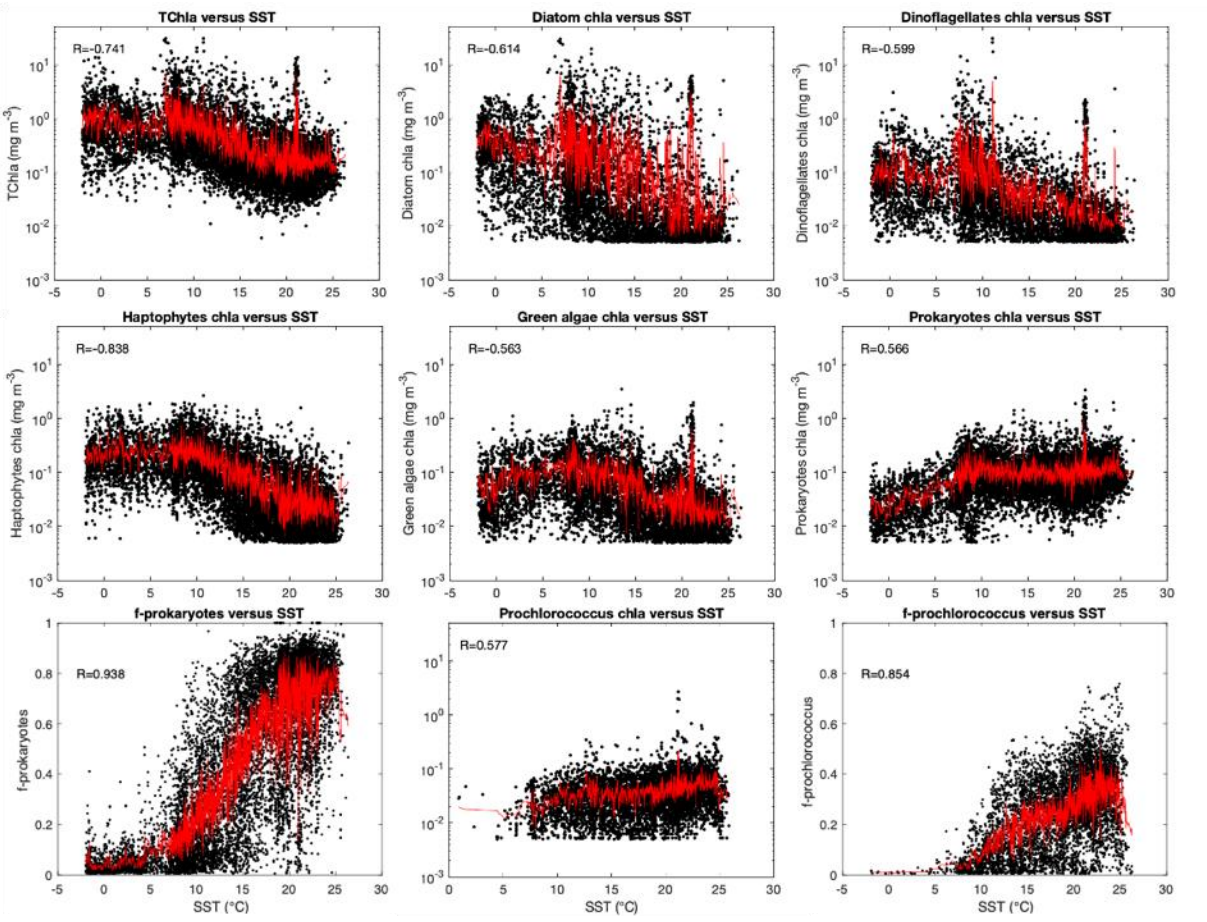

Figure 3. Scatterplots of *in situ* TChl-a, PFT Chl-a and fractions of prokaryotes and *Prochlorococcus versus* collocated satellite SST data. The correlation coefficient R was calculated based on the 10-point running mean (red curve).

2.2.1 Adapted EOF-SST hybrid PFT algorithm based on the whole data set

The input data set used in the EOF-SST hybrid algorithm was the matchup data set that included the collocated nine-band Rrs from the merged products, SST satellite data and *in situ* PFT data. Figure 4 depicts the flowchart of the EOF-SST hybrid algorithm, in which the EOF

analysis remained unchanged by still using singular value decomposition (SVD) to decompose the (standardized) Rrs spectra into the EOF scores (U), singular values (Λ) and EOF loadings (V) as in Xi *et al.* (2020). Now, when formulating the regression models of PFTs, we introduced SST as an additional term together with the column vectors $u_{1,2,..,n}$ in U. Similar to Xi *et al.* (2020), we applied a stepwise routine to obtain the smaller regression model by removing least significant variables in U through minimization of the Akaike information criterion (AIC). The adapted regression model is expressed as

$$\ln(C_{\mathrm{p}}) = a_0 + a_1 u_1 + a_2 u_2 + \cdots a_n u_n + a_{SST} SST, \quad (1)$$

where a_0 is the intercept, $a_{1,2,\ldots n}$, and a_{SST} are the regression coefficients for the selected EOF scores and SST, respectively. With the adapted regression model, the same steps described as cross validation and model assessment of Xi *et al.* (2020) were carried out to test the robustness of the fitted model: the whole collocated data set was randomly split into two subsets – the first subset containing 80% of the data was used for model fitting/training and the rest 20% was used for prediction. The procedure was run for 500 permutations to 1) record down in each permutation the model parameters for further uncertainty assessment, and 2) generate a final statistical assessment based on the statistics of the model performance derived from each permutation.

For the model assessment, we considered the slope (*S*), the intercept (*a*) of the GLM regression and coefficient of determination (R^2), which were based on the log-scaled PFT predictions against the log-scaled *in situ* PFT data. We also included the root-mean-square difference (RMSD), the median percent difference (MDPD), and the bias that were based on the non-log-transformed concentration data. These metrics were expressed as

$$\mathrm{RMSD} = \sqrt{\frac{\sum_{i=1}^{M}(C_{pi}-C_{oi})^2}{M}}, \quad (2)$$

$$\mathrm{MDPD} = \mathrm{Median\ of}\ \left[\frac{|(C_{pi}-C_{oi})|}{C_{oi}} \times 100\right],\ \mathrm{i} = 1,\ldots M, \quad (3)$$

$$\mathrm{bias} = \frac{100}{M}\sum_{i=1}^{M}\frac{(C_{pi}-C_{oi})}{C_{oi}}, \quad (4)$$

where *M* is the number of observations of PFTs (C_{o}) and the corresponding predictions (C_{p}). Meanwhile, the cross validation statistics (R^2cv, RMSDcv and MDPDcv), which represent both the model robustness and compromise model performance, was also determined by taking the mean of the statistical parameters R^2, RMSD and MDPD from all permutations, respectively.

2.2.2 SST-separated hybrid PFT algorithms

Given the presented different SST-PFTs relationships for data set of SST < 8 °C and that of SST ≥ 8 °C (Figure 3), for all PFT quantities but *Prochlorococcus* Chl-a and fraction we separated the matchup data set based on 8 °C and established two specific EOF-SST hybrid algorithms using the two data sets (noted as SST-separated hybrid algorithms) following Section 2.2.1 (Figure 4). Note that the performance of the SST-separated hybrid algorithms was evaluated statistically based on all the predictions and *in situ* data to be consistent with that for the EOF-SST hybrid algorithm.

2.2.3 Application of algorithms

The established algorithms were applied to the satellite R_{rs} data from the merged products (Section 2.1.2) to retrieve PFTs globally (Figure 4). By projecting the R_{rs} data from the satellite onto the EOF loadings (V), a new set of EOF scores (U^{sat}) was derived and was then used for the global PFT prediction together with the SST as an additional term in the fitted model in Eq. (1), where a_0 and $a_{1,2,...n}$ were obtained in the step of model training.

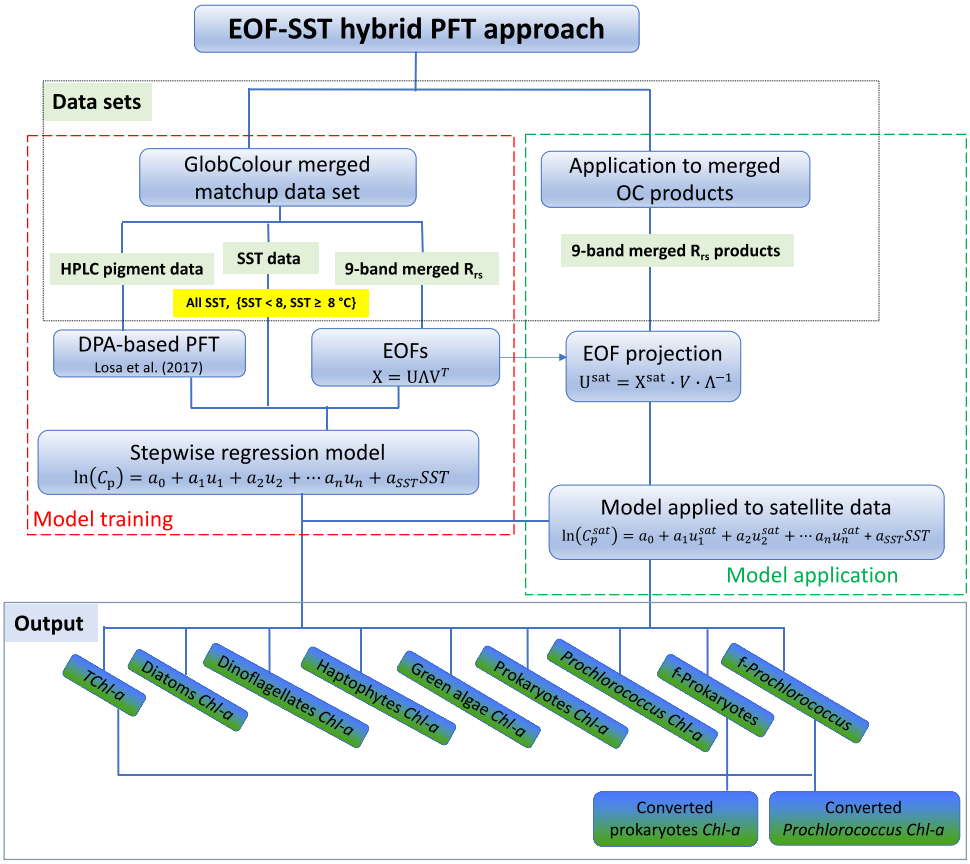

Figure 4. Flowchart illustrating the EOF-SST hybrid algorithm and the SST-separated hybrid algorithms for predicting TChl-a, Chl-a of six PFTs, and two fractions with GlobColour

merged product. The red dashed-line box depicts the model training with the pigment-satellite matchup data; the green dashed-line box depicts the model application to satellite products and the blue dashed-line box shows the output, i.e., the predicted PFT quantities.

2.3 Uncertainty assessment of PFT retrieval

To quantify the uncertainty of the satellite PFT retrievals, we considered the uncertainties propagated from the input datasets satellite R_{rs} (σ_{Rrs}) and SST (σ_{SST}), and uncertainty of the model/algorithm parameters (σ_a). Also other uncertainty sources exist, i.e., errors in the DPA derived PFT data which results from the incorrect assignment of PFTs from marker pigments and the *in situ* HPLC pigment measurement error. We were not able to obtain this information for our large global data set collected from various cruises in the last decades. Mostly no other descriptors of phytoplankton taxonomic composition had been measured and details on the HPLC measurement error (including all associated steps, e.g., filtration, extraction and HPLC analysis accuracy) are not available. According to IOCCG (2019), uncertainties of the HPLC-based chlorophyll a is around 7% and can be higher for other pigments (Claustre *et al.*, 2004). In the current study, we could not quantify the combined uncertainty from both, HPLC measurement and the DPA derived PFT, due to limited information therefore did not include this error source in the uncertainty assessment.

All computations of the uncertainties in this study were based on the logarithmic transformed data following conventional practice in the field of ocean color (OCCCI Product User Guide, 2020). However, we used natural logarithms instead of the common (base 10) logarithms, because our algorithm was developed based on the natural logarithms. The common logarithmic uncertainty can also be obtained by dividing our uncertainty by ln(10), i.e., approximately a factor of 2.3. Due to the length of the article only the uncertainty derived based on the whole EOF-SST hybrid algorithm is presented as a general approach to quantify and consolidate the PFT uncertainty from different error sources.

2.3.1 Structure of the uncertainty propagation

With the EOF-SST hybrid retrieval models expressed in Eq. (2), the retrieval model applied to the satellite data can be written in the following form:

$$y(\boldsymbol{a}, \boldsymbol{u}(Rrs), SST) = \ln(C_P^{sat}) = a_o + a_1 u_1^{sat} + a_2 u_2^{sat} + \cdots a_n u_n^{sat} + a_{SST} SST \quad (5)$$

where $\boldsymbol{a}$ represents all the model coefficients; $\boldsymbol{u}$ represents all the EOF score vectors derived from R_{rs} data therefore each can be expressed as:

$$u_i^{sat} = f(Rrs) \quad (6)$$

To estimate the final uncertainty of the retrieved PFTs, σ_y, we assume that the uncertainties due to ***a***, ***u***, and SST in Eq. (5) are not correlated with each other. According to the Guide to Uncertainty in Measurement (JCGM, 2008), the combined uncertainty of different sources could be estimated based on the law of propagation of uncertainty. Using the partial differences, the uncertainty of the PFT retrievals is presented theoretically as:

$$\sigma_y = \sqrt{\sigma_{y(Rrs)}^2 + \sigma_{y(a)}^2 + \sigma_{y(SST)}^2} = \sqrt{\sum_{i=1}^{N}\left(\frac{\partial y}{\partial Rrs_i}\right)^2 \sigma_{Rrs_i}^2 + \sum_{i=0}^{n}\left(\frac{\partial y}{\partial a_i}\right)^2 \sigma_{a_i}^2 + \left(\frac{\partial y}{\partial SST}\right)^2 \sigma_{SST}^2}\,. \quad (7)$$

Since the uncertainties propagated from errors of model parameters ($\sigma_{y(a)}$) and SST ($\sigma_{y(SST)}$) are both linear, they can be analytically derived and expressed together as:

$$\sigma_{y(a)}^2 + \sigma_{y(SST)}^2 = \sum_{i=1}^{N}(u_i^{sat})^2\sigma_{a_i}^2 + SST^2\sigma_{a_{sst}}^2 + (a_{sst})^2\sigma_{SST}^2. \quad (8)$$

Where σ_{SST} = 0.46 °C (Worsfold *et al.*, 2020 for the OSTIA SST product); σ_{a_i} and $\sigma_{a_{SST}}$ were determined during the cross validation procedure as described in Section 2.2.1. To further understand how the σ_{a_i} and $\sigma_{a_{SST}}$ were determined, Figure 5 shows the distributions of the coefficients derived from all the permutations in the cross validation as an example for diatoms. In general, the coefficient distributions followed the normal distribution, the uncertainty of each coefficient was thus determined by calculating the corresponding standard deviation. The uncertainties of the model coefficients for all other PFT quantities were also determined in the same manner.

Since the converted prokaryotes and *Prochlorococcus* Chl-a were calculated by multiplying their fractions and the TChl-a together, the corresponding uncertainties were determined by the uncertainties of TChl-a and that of *f*-Prokaryotes (*f-Prochlorococcus*). Using $y_{\text{proka\_conv}}$, y_1 and y_2 to denote the converted prokaryotes Chl-a, TChl-a and f-Prokaryotes, the uncertainty of the converted prokaryotes Chl-a, $\sigma_{y_{proka\_conv}}$, can be determined by the uncertainty of TChl-a and *f*-Prokaryotes, namely σ_{y_1} and σ_{y_2}, through the following equation:

$$\sigma_{y_{proka\_conv}} = \sqrt{\sigma_{y_1}^2 + \sigma_{y_2}^2 + 2\sigma_{y_1}\sigma_{y_2}r_{12}}, \quad (9)$$

where r_{12} is the correlation coefficient between σ_{y_1} and σ_{y_2} (as both depend on SST-related uncertainties). Eq. (9) also applies for the uncertainty of converted *Prochlorococcus* Chl-a.

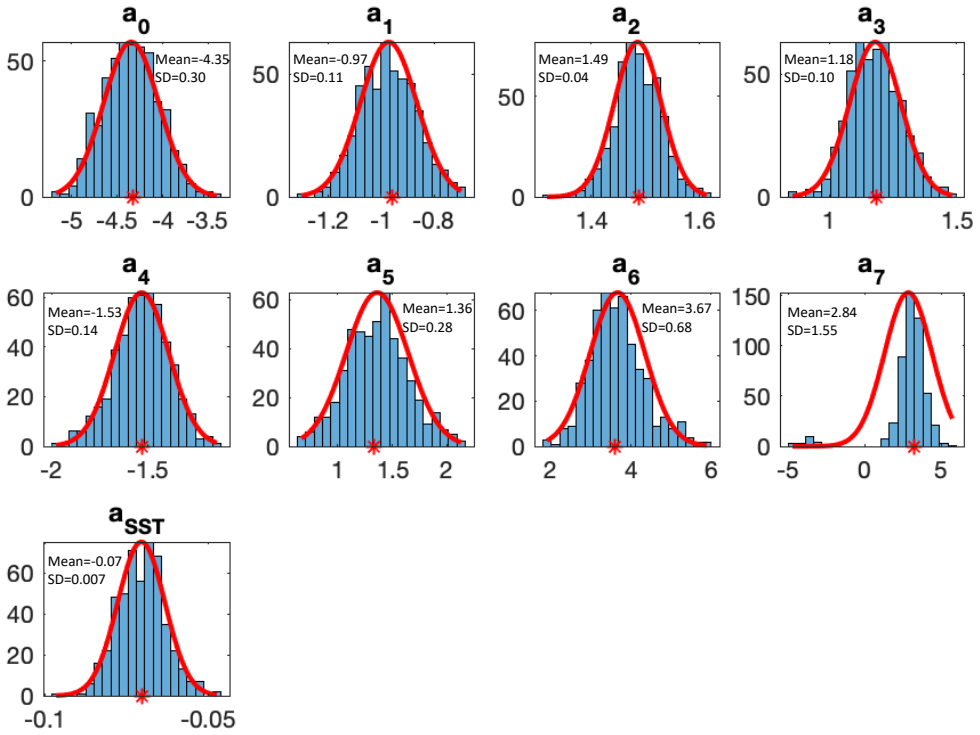

Figure 5. Histograms depicting the distributions of the model coefficients derived from 500 permutations of the cross validation for diatoms. σ_{a_i} (i.e., standard deviation, SD) of each coefficient was determined accordingly.

Among all uncertainty components in Eq. (7), the uncertainty of the PFTs propagated from the errors of the satellite Rrs spectra, $\sigma_{y(Rrs)}$, is the challenging part to quantify, as it is nonlinear and not as straightforward as the other two uncertainty sources, due to the EOF analysis performed with the spectra. We therefore used a MC simulation-based approach to estimate the $\sigma_{y(Rrs)}$ and detailed it in the following subsection 2.3.2.

2.3.2 Rrs uncertainty propagation

Based on the uncertainty of the water leaving radiance for SeaWiFS, MODIS-Aqua, and MERIS reported in Maritorena *et al.* (2010), Rrs absolute uncertainties for these sensors were derived and were used in GlobColour program. In our study, we took the root mean square (RMS) of the common bands from two or three sensors as the uncertainty of the merged products (Table 2). Using the matchup data for the merged products at nine bands, the following steps were carried out to fulfil the uncertainty propagation from Rrs to the PFTs.

1. The 508 Rrs matchup spectra were randomly divided equally into two datasets - 50% as the training data set, and the other 50% as the testing data set (in a total of 254).

The corresponding matchups of *in situ* PFT and retrieved PFT data were also divided accordingly.

2. For the training data sets, we performed 10,000 MC simulations to randomly introduce for each band the Rrs uncertainty (σ_{Rrs}) to each Rrs spectrum in the training data set (in a total of 2,540,000 simulated spectra).
3. The MC simulated Rrs spectra were applied to the EOF-SST hybrid algorithm to estimate the PFTs with Rrs uncertainty taken into account. For each sample, 10,000 estimates of the PFT were generated from the 10,000 MC simulated Rrs, so that the uncertainty (standard deviation, $\sigma_{MC\text{-}PFT}$) of the PFTs were determined based on these 10,000 estimates for each specific sample.
4. When the σ_{MC} for all samples in the training data set were determined through Step 3, a look-up table (LUT) was built for each PFT by fitting $\sigma_{MC\text{-}PFT}$ as a function of the retrieved PFT.
5. The LUT for each PFT was applied to the testing data set for the uncertainty validation, and also to the satellite PFT products to derive per-pixel uncertainty of the satellite PFT due to Rrs, $\sigma_{y(Rrs)}$, which was combined with uncertainties from the other sources via Eq. (7) to derive the final uncertainty of PFT satellite retrievals.

Table 2. Absolute uncertainties of Rrs (σ_{Rrs}, Sr^{-1})) for different sensors in the merged products derived based on Maritorena *et al.* (2010). The root mean square (RMS) was taken as the uncertainty of the merged products.

Wavebands (nm)	412	443	490	510	531	547	555	670	678
MODIS σ_{Rrs}	0.00071	0.00063	0.00049	-	0.00024	0.00019	-	0.000055	0.000030
MERIS σ_{Rrs}	0.00066	0.00059	0.00047	0.00033	-	-	0.00023	0.00010	0.000098
SeaWiFS σ_{Rrs}	0.00072	0.00064	0.00050	0.00036	-	-	0.00025	0.000075	-
RMS σ_{Rrs}	0.00070	0.00062	0.00049	0.00035	0.00024	0.00019	0.00024	0.000080	0.000072

2.3.3 Assessment of the per-pixel PFT uncertainty

With the steps in Section 2.3.2, the uncertainty propagated from the Rrs to the satellite retrieved PFTs was determined by applying the LUT to each pixel of the satellite derived PFT products, the term $\sigma^2_{y(Rrs)}$ in Eq. (7) was thus derived. Together with the other two terms, $\sigma^2_{y(a)}$ and $\sigma^2_{y(SST)}$ that could be calculated analytically through Eq. (8), the combined PFT uncertainty σ_y of each pixel from different sources was ultimately obtained.

3 Results and discussion

3.1 EOF-SST hybrid algorithms for PFT retrievals

3.1.1 EOF-SST hybrid algorithm based on the whole matchup data set

Before setting up the EOF-SST algorithm, we firstly used the updated input data set to update the original EOF-based algorithm proposed by Xi *et al.* (2020) where SST was not included, the performance of the updated algorithm showed nearly identical performance as compared to the original one presented in Xi *et al.* (2020) (details not shown). This indicates that the original algorithm can be hardly improved by purely enlarging the training data set. Within the frame of the EOF-SST hybrid algorithm in the current study, TChl-a, PFT Chl-a and the fractions of two PFTs were predicted based on the regression models built using the EOF scores derived from the nine-band Rrs data, SST and the *in situ* PFT data. As presented in Table 3 and Figure 6 (A-F, H), compared to the original algorithm in Xi *et al.* (2020), the EOF-SST hybrid algorithm shows significant improvements for all predicted quantities except for *Prochlorococcus* where weak performance still remains. For TChl-a, and Chl-a for diatoms, haptophytes, dinoflagellates and green algae, R^2 and R^2cv are increased to 0.59 – 0.85 (compared to 0.51 – 0.76) and to 0.56 – 0.84 (compared to 0.47 – 0.75), respectively. MDPD and MDPDcv are remarkably reduced to 30% to 55% and 31% to 56%, respectively, for all quantities as compared to Xi *et al.* (2020) ranging 37%–74% and 37%–75%, respectively. RMSD and RMSDcv values are also decreased significantly in the EOF-SST hybrid algorithm compared to the previous results.

To further improve the prediction of prokaryotes and *Prochlorococcus* Chl-a, the hybrid algorithm was also trained to retrieve the fractions of prokaryotes and *Prochlorococcus* to TChl-a. This was motivated because prokaryotes dominate the low TChl-a mid- to low latitude waters, so generally their Chl-a is low. By using their fraction instead of Chl-a a better spread of the data is achieved that enhances the signal to be retrieved which is beneficial for application in abundance-based PSC retrievals (e.g., Brewin *et al.*, 2010). As expected, the prediction models for the two fractions performed well with $R^2 > 0.62$ and MDPD within 42% (Table 3). Though the overall performance of the fraction retrieval for the two PFTs had been improved, the regressions between the predicted and observed fractions (Figure 6G and J) show that higher discrepancies exist in low fraction values, indicating that it is still difficult to deal with low Chl-a values. Using predicted TChl-a, the fractions were further converted to Chl-a for the two PFTs. Table 3 shows that the converted prokaryotes

Chl-a retrieval displays much improved performance compared to the directly retrieved prokaryotes (R^2 of 0.34 vs. 0.27, MDPD of 39% vs. 44%, and RMSD of 0.08 vs. 0.09 mg m^{-3}), but it is downgraded compared to the *f*-prokaryotes (Figure 6H). The fraction to Chl-a conversion scheme shows barely improvement in predicting *Prochlorococcus* Chl-a (Table 3 and Figure 6K versus Figure 6I). Though *f-Prochlorococcus* is overall better predicted compared to the direct retrieval of *Prochlorococcus* Chl-a, by using the conversion, the low signal to noise ratio in the retrieved TChl-a and *f-Prochlorococcus* deteriorates for R^2 and RMSD the final *Prochlorococcus* Chl-a estimation. The MDPD and bias are however slightly improved. Weak prediction performance of the converted *Prochlorococcus* Chl-a reveals that it is still challenging to enhance their retrieval accuracy to the same level as other PFTs due to the low concentrations and small variability (Xi *et al.*, 2020).

Table 3. Statistics of regression models for TChl-a, six PFT Chl-a, fractions of prokaryotes and *Prochlorococcus* and the corresponding converted Chl-a using SST and EOF modes based on the nine-band Rrs matchups from merged OC products (upper panel). N is the number of valid matchups for each parameter. Note that cross validation was not applied for the converted prokaryotes and *Prochlorococcus* Chl-a because they are the results of the multiplication between their fractions and the TChl-a. As a comparison, the statistics of the previous EOF-based algorithm (without SST) by Xi *et al.* (2020) for the TChl-a and six PFT Chl-a are also presented (lower panel). Bold marks the improved (or same) statistics.

	N	MDPD (%)	RMSD (mg m^{-3})	R^2	MDPDcv (%)	RMSDcv (mg m^{-3})	R^2cv
EOF-SST hybrid model							
TChl-a	412	**30.02**	**0.85**	**0.85**	**30.60**	**0.88**	**0.84**
Diatoms	296	**54.90**	**0.95**	**0.79**	**56.46**	**1.05**	**0.78**
Dinoflagellates	250	**51.44**	0.95	**0.64**	**53.81**	**0.70**	**0.60**
Haptophytes	402	**40.24**	**0.16**	**0.73**	**41.96**	**0.16**	**0.72**
Green algae	285	**48.64**	**0.10**	**0.59**	**49.71**	**0.11**	**0.56**
Prokaryotes	395	**44.37**	**0.09**	**0.27**	**44.79**	**0.09**	**0.22**
f-Prokaryotes	395	40.90	0.20	0.66	41.91	0.20	0.65
Converted Prokaryotes	391	**39.36**	**0.08**	**0.34**	-	-	-
Prochlorococcus	195	41.41	0.02	**0.26**	44.22	0.02	**0.19**
f-Prochlorococcus	201	41.08	0.10	0.62	42.07	0.10	0.58
Converted Prochlorococcus	190	39.74	0.02	0.21	-	-	-
Original EOF based algorithm							
TChl-a	394	37.41	1.24	0.76	37.08	1.27	0.75
Diatoms	306	73.70	1.21	0.65	74.74	1.29	0.63
Dinoflagellates	272	55.32	0.93	0.62	57.29	0.72	0.59
Haptophytes	387	47.16	0.22	0.64	48.62	0.24	0.61
Green algae	262	55.81	0.11	0.51	56.26	0.11	0.48
Prokaryotes	367	53.70	0.13	0.15	55.08	0.13	0.11
Prochlorococcus	142	39.65	0.02	0.24	42.68	0.02	0.18

448

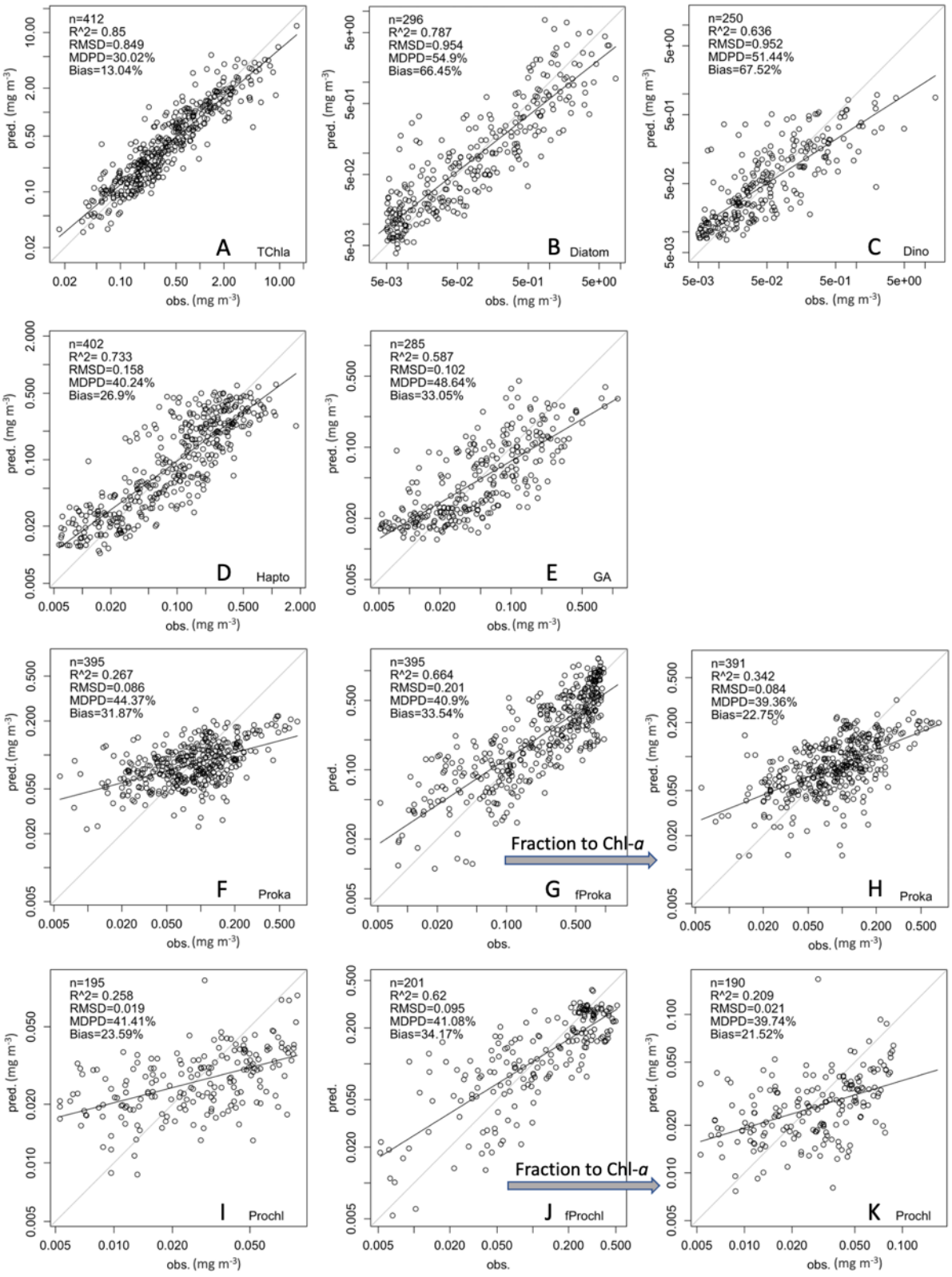

449

450 Figure 6. Regressions between observed (x-axis, obs.) and predicted (y-axis, pred.) PFT
451 quantities using EOF-SST hybrid algorithm: (A) TChl-a, (B) diatoms, (C) dinoflagellates, (D)
452 haptophytes, (E) green algae, (F) prokaryotes, (G) *f*-prokaryotes, (H) converted prokaryotes

Chl-a from *f*-prokaryotes, (I) *Prochlorococcus*, (J) *f-Prochlorococcus*, and (K) converted *Prochlorococcus* Chl-a from *f-Prochlorococcus*.

3.1.2 SST-separated hybrid algorithms for different SST regimes

According to Section 2.2.2, SST-separated hybrid algorithms were performed to retrieve the PFT quantities respectively for the two temperature regimes. Tables 4 summarizes the coefficients fitted in the stepwise regression models based on the whole data set, data set with SST $\geq$ 8 °C, and data set with SST < 8 °C, respectively. EOF modes chosen for different PFTs vary with different data sets, and that SST, as an additional regression term, may not always been used in the final prediction models. The term had been identified as insignificant within the stepwise minimization method routine performed in the model regression procedure (Xi *et al.*, 2020). Moreover, the weighting (coefficient) fitted on the SST term changed when different data sets were used. For instance, a_{SST} fitted in the prediction models for prokaryotes using the whole data set was 0.065, and was enhanced to 0.177 for the data set with SST < 8 °C, but was not used in the prediction model for the data set with SST $\geq$ 8 °C which is also consistent with the SST-PFT relationship (Figure 3). The 10-point running mean trend showed that SST had a distinct positive correlation with the prokaryotes Chl-a but the correlation turned insignificant when SST was higher than 8 °C.

As shown in Table 5 and Figure 7, the improvement for TChl-a in the SST-separated algorithms is rather small, indicating that responses in the TChl-a concentration to different SST regimes is relatively stable. For predictions of Chl-a of all PFTs, but *Prochlorococcus* for which the separation of SST does not apply, the SST-separated algorithms perform much better, indicated by improved statistics in terms of R^2, RMSD and MDPD (Table 5). Prokaryotes, both in quantities of Chl-a and fraction, show the most promising output compared to that from the previous settings. With good performances in retrieving the *f*-prokaryotes and TChl-a, again, the prokaryotes Chl-a is also better derived through converting the fraction to concentrations (Figure 7H) compared to the directly retrieved prokaryotes Chl-a (Figure 7F), with an increase of R^2 from 0.34 to 0.43 and reduced MDPD from 39.36% to 36.51%. Even though prokaryotes retrieval is still not as good as the other PFTs such as diatoms and haptophytes, this is already a significant improvement after a series of experiments by including SST in the retrieval model, establishing separated models based on SST regimes, and retrieving firstly the fraction and performing the conversion.

Table 4. Coefficients of the EOF-SST based regression models for the merged products used to predict TChl-a, PFT Chl-a and two PFT fractions using data sets with SST ≥ 8 °C only, SST < 8 °C only, and all SST, respectively. Note that TChl-a prediction models are based on the EOFs derived from original Rrs spectra but the others are based on the standardized Rrs spectra.

		N	Intercept	EOF1	EOF2	EOF3	EOF4	EOF5	EOF6	EOF7	EOF8	SST
TChl-a	SST≥8°C	353	0.570	154.542	128.794	936.120	-668.923	-275.773	1014.797			-0.017
	SST<8°C	59	0.400	91.507	328.418	777.466	-1263.425			-1422.531		
	all SST	412	0.518	143.568	155.376	913.763	-766.036	-225.255	859.576			-0.019
Diatoms	SST≥8°C	239	-5.823	-1.086	1.783	1.346	-1.362	1.713	3.978	2.992		
	SST<8°C	57	-2.351	-0.724	0.922	0.387	-1.621	1.176	3.236			-0.192
	all SST	296	-4.322	-0.961	1.487	1.184	-1.530	1.334	3.598	3.250		-0.070
Dinoflagellates	SST≥8°C	200	-4.166	-0.561	1.055	0.518	-1.129					-0.032
	SST<8°C	50	0.499	1.410	0.578	1.219	-1.834		2.113	7.895		0.085
	all SST	250	-4.753	-0.665	1.111	0.566	-1.206	0.921			-5.563	
Haptophytes	SST≥8°C	343	-4.171	-0.914	1.037		-0.591	-1.279				-0.056
	SST<8°C	59	-3.415	-0.564	0.286	0.522	-1.323	-1.783	-1.930	-3.888		0.049
	all SST	402	-4.983	-1.155	1.061	0.202	-0.714	-0.880		1.314	-2.285	-0.035
Green algae	SST≥8°C	244	-2.930		0.706	0.285	-0.566	-1.858	-1.115	2.322		-0.022
	SST<8°C	41	-3.412		0.478	0.427		-1.484				0.128
	all SST	285	-3.166		0.729	0.235	-0.472	-1.812	-1.631	2.339		
Prokaryotes	SST≥8°C	343	-2.410		0.156	0.390		-2.138	-1.039	-1.969		
	SST<8°C	52	-4.052		0.169	0.687	0.952	-1.561	-2.631	8.019		0.177
	all SST	395	-3.396		0.295	0.379	0.322	-2.090	-2.187	-2.072		0.065
f-prokaryotes	SST≥8°C	342	0.156	0.703	-0.903	-0.396	0.824	-2.081	-3.082	-4.976		0.032
	SST<8°C	53	-1.775	0.689	-0.360		2.061	-2.575	-5.499	8.041		0.124
	all SST	395	-0.945	0.658	-0.698	-0.285	1.034	-1.915	-3.621	-4.659		0.089
Prochlorococcus	SST≥8°C	195	-4.088		0.114			-3.043	-1.619	-3.848		0.028
f-Prochlorococcus	SST≥8°C	201	0.156	0.846	1.184	-0.654	0.564	-2.723		5.067		

Table 5. Combined statistics of the regression models from the SST-separated hybrid algorithms for matchup data set with SST ≥ 8 °C and that with SST < 8°C. Improved parameters are marked as bold, by comparing to those from the hybrid algorithm without separating SST (Table 3).

	N	**R^2**	**RMSE**	**MDPD (%)**
TChl-a	412	**0.86**	**0.84**	30.21
Diatoms	296	**0.82**	**0.93**	**49.89**
Dinoflagellates	250	**0.66**	**0.73**	**50.23**
Haptophytes	402	**0.76**	**0.15**	**39.53**
Green algae	285	**0.61**	0.10	**44.37**
Prokaryotes	395	**0.35**	**0.08**	**40.85**
f-Prokaryotes	395	**0.72**	**0.17**	**33.60**
Converted prokaryotes	395	**0.43**	0.08	**36.51**

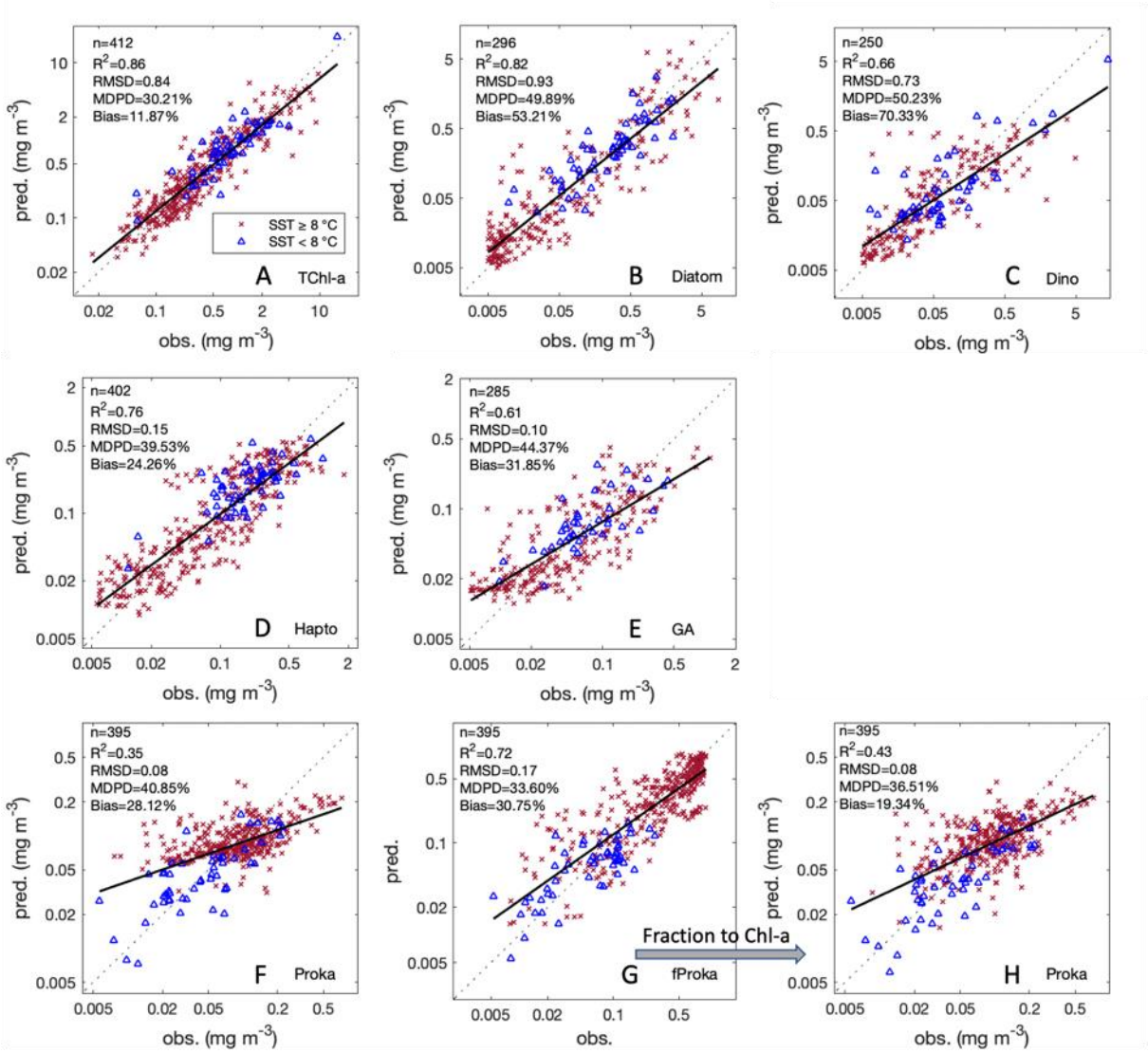

Figure 7. Combined regressions between observed (x-axis, obs.) and predicted (y-axis, pred.) PFT quantities from two sets of EOF-SST hybrid algorithms based on different SST ranges: (A) TChl-a; Chl-a of (B) diatoms, (C) dinoflagellates, (D) haptophytes, (E) green algae, and (F) prokaryotes; (G) *f*-prokaryotes and (H) converted prokaryotes Chl-a from *f*-prokaryotes. The dotted black line shows the 1:1 line and the solid black line indicates the regression based on the whole data set.

3.2 Global maps of PFT quantities from merged Rrs products

The improved EOF-SST hybrid algorithms were applied to the merged Rrs and SST products to derive the global TChl-a, PFT Chl-a concentrations and the fractions (see Figure 4, part model application). To illustrate the global distribution of the PFTs, Figures 8-9 show as example the annual mean generated from the derived monthly PFT quantities (except *Prochlorococcus*) for the year of 2011 using the EOF-SST hybrid algorithm (established in Section 2.2.1) and the SST-separated algorithms (established in Section 2.2.2), respectively,

with the absolute difference between these two products. Since *Prochlorococcus* barely exist at cold temperatures (cf. Section 2.2), global maps of *Prochlorococcus* Chl-a and f-*Prochlorococcus* are generated only for regions with SST ≥ 8 °C (Figure 10).

In general, distribution patterns of the retrieved TChl-a and the four eukaryotic PFTs from the EOF-SST hybrid algorithm are consistent with that from the combination of the SST-separated algorithms (Figure 8). However, distinct differences between the retrievals from the two approaches are found in the polar regions (Figure 8K-O). Compared to that from the EOF-SST hybrid algorithm, TChl-a concentrations derived from SST-separated algorithms are elevated in most regions of the Southern Ocean compared to that from EOF-SST hybrid algorithm, while slightly decreased in the Arctic except for the Greenland Sea and Barents Sea (Figure 8A versus 8F). Diatoms Chl-a from the SST-separated approach is enhanced in the high latitudes and waters near the coasts (Figure 8G versus Figure 8B). Haptophytes Chl-a is also found enhanced mostly in the moderately high latitudes (e.g., 50°S to 60°S near polar fronts) and decreased in very high latitudes and marginal seas using the SST-separated algorithms (Figure N). The Chl-a for dinoflagellates and green algae are generally slightly lower in most of the oceans except for the Southern Ocean near the polar fronts where higher concentrations are observed in the SST-separated algorithms (Figures M&O). Compared to the retrievals of Xi *et al.*, (2020) with detailed inter-comparison among different PFT/PSC products, these satellite derived PFTs from the SST-separated algorithms are in better agreement with the equivalent products from other studies (e.g., Hirata *et al.*, 2011; Losa *et al.*, 2017; Brewin *et al.*, 2015).

The retrievals of prokaryotes Chl-a, *f*-prokaryotes and the converted prokaryotes Chl-a using SST-separated algorithms present generally lower Chl-a and fraction for prokaryotes globally except in the regions around 40 °S in the southern hemisphere, 40 °N in the north Pacific Ocean and between 45 °N and 65 °N in the north Atlantic Ocean (Figure 9G-I). The converted Chl-a from fraction shows more reasonable global distribution (Figure 9C and F) compared to the direct retrievals (Figure 9A and D), given the improved performance via fraction conversion for prokaryotes in Section 3.1. However, the EOF-SST hybrid algorithm derived *f*-prokaryotes is saturated (up to 1) in most mid- to low latitudes (Figure 9B). This saturation is remarkably reduced by the SST-separated algorithms (Figure 9E) thanks to the better description of the prokaryotes' dependency on the temperature in the algorithm, resulting in that converted Chl-a from SST-separated algorithms (Figure 9F) has the most reliable retrieval quality among all prokaryotes Chl-a retrievals shown in Figure 9. Compared

to the prokaryotes retrieval in Xi *et al.* (2020), where the original EOF-based algorithm overestimates the prokaryotes Chl-a dramatically, the converted prokaryotes Chl-a in this study shows better agreements with previous retrievals (Hirata *et al.*, 2011; Losa *et al.*, 2017) but is lower in the polar regions. Validation with in situ data is necessary when more measurements are available in the future.

Regarding *Prochlorococcus*, though the fraction converted Chl-a showed no distinct improvement in model performance compared to the direct Chl-a retrieval (Section 3.1.1), the global retrieval depicts the overall decrease in the converted Chl-a by *f-Prochlorococcus* (Figure 10C) compared to the direct retrieval (Figure 10A), which considerably agrees to what we expect from in-situ and other satellite retrievals (Hirata *et al.* 2011, Alvain *et al.* 2008). The conversion to Chl-a is therefore also restricted by the high uncertainty at low TChl-a and also the low variability of *Prochlorococcus* Chl-a (Xi *et al.*, 2020).

In summary, we consider that the SST-separated algorithms perform better than the EOF-SST hybrid algorithm and the original EOF-based algorithm by Xi *et al.* (2020) for global PFT retrievals. Especially for the prokaryotic phytoplankton distributions show more contrasting patterns between gyre and non-gyre regions, and TChl-a and diatom Chl-a are higher in the Southern Ocean where often satellite-derived estimates have shown too low values (e.g., Johnson *et al.*, 2013; Soppa *et al.*, 2014).

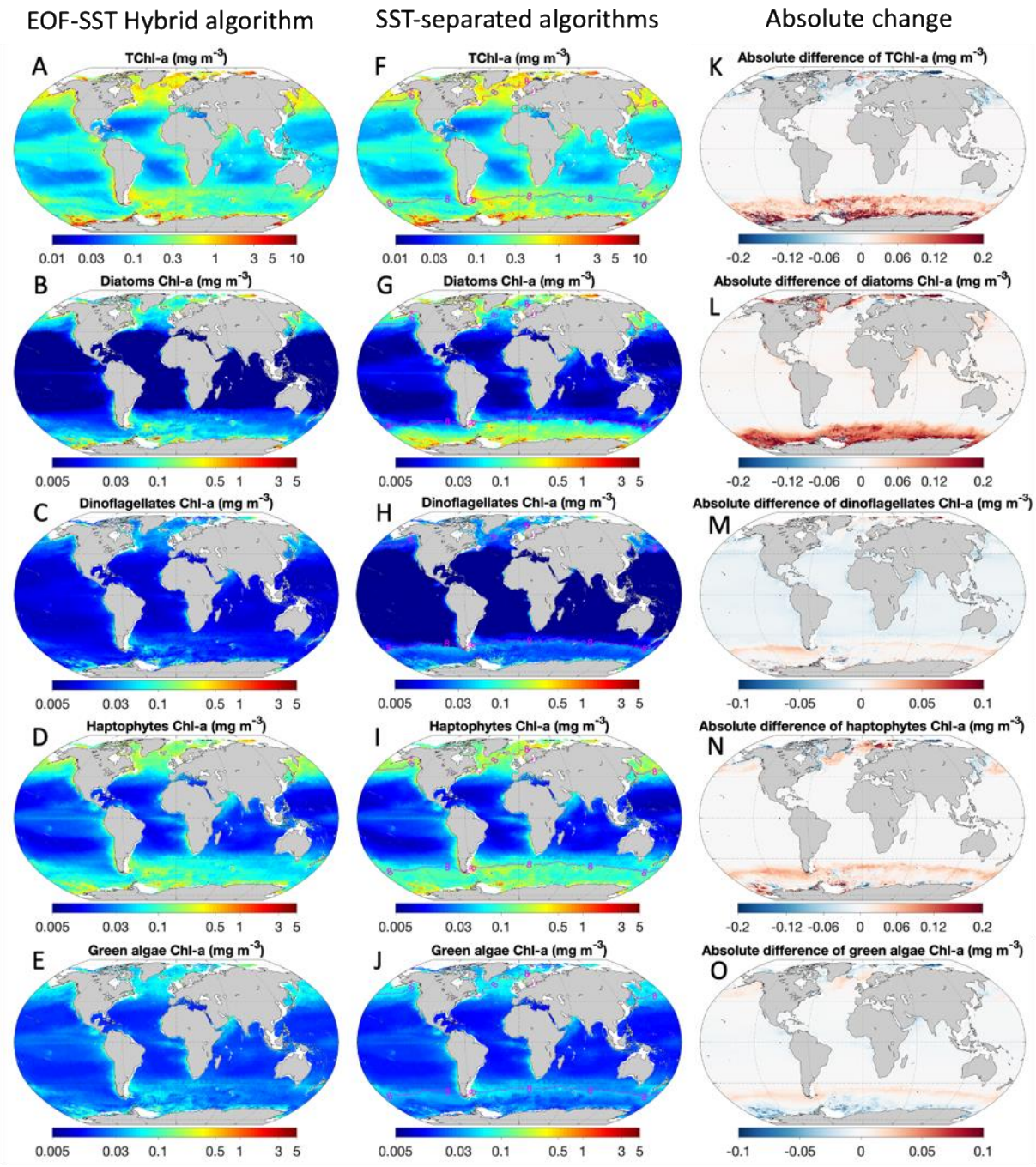

Figure 8. Satellite derived estimates of annual (2011) mean surface TChl-a, Chl-a of diatoms, dinoflagellates, haptophytes, and green algae. Panels (A-E): EOF-SST hybrid algorithm with non-separated SST; Panels (F-J): Combined estimates from SST-separated hybrid algorithms for SST $\geq$ 8 °C and SST < 8 °C, respectively. The magenta curve indicates the isotherm of 8 °C. Panels (K-O): Absolute difference between the combined estimates from SST-separated algorithms and that from EOF-SST hybrid algorithm, i.e. panel (F-J) minus panel (A-E).

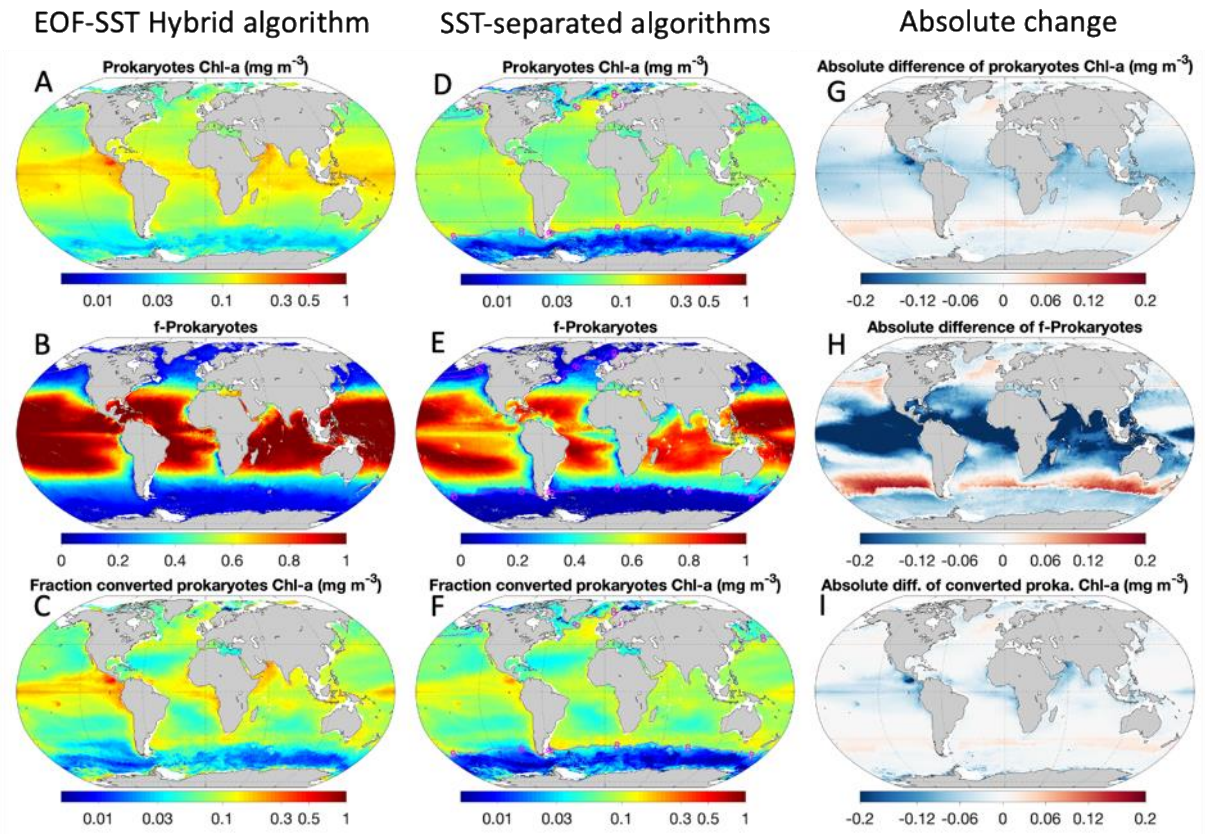

Figure 9. Same as in Figure 8 but for mean surface Chl-a of prokaryotes, *f*-prokaryotes and the converted prokaryotes Chl-a.

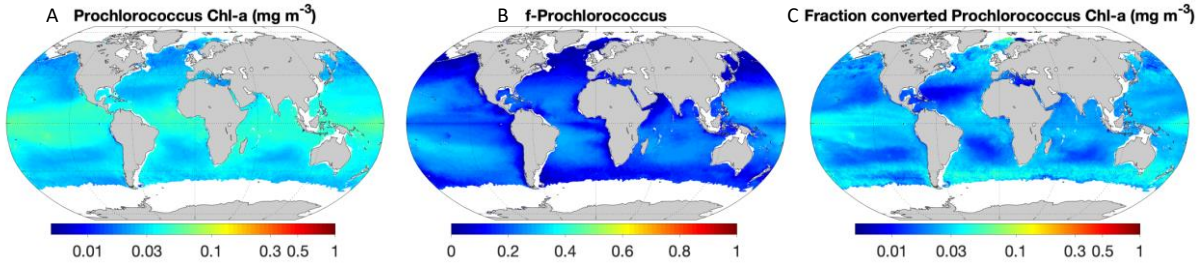

Figure 10. Satellite derived estimates of annual (2011) mean surface (A) Chl-a of *Prochlorococcus*, (B) *f-Prochlorococcus*, and (C) the converted *Prochlorococcus* Chl-a using the EOF-SST hybrid algorithm.

3.3 PFT uncertainty

3.3.1 Look-up table (LUT) for uncertainty due to Rrs

Following the steps listed in Section. 2.3.2 to build the look-up table (LUT) for quantifying PFT uncertainty propagated from Rrs uncertainty, Figure 11 and Table 6 show the regressions and the statistical results of $\sigma_{MC\text{-}PFT}$ against the originally predicted PFT quantities. Higher R^2 and lower RMSD are achieved in general when higher degree of polynomial is used (Table 6).

582 However, the difference between different regressions is rather small except for diatoms and
583 dinoflagellates, which are caused by their few data points at higher concentrations with
584 corresponding lower MC derived uncertainties (Figures 11B-C). To be conservative, linear
585 regressions were taken as the final LUT functions to determine $\sigma_{y(Rrs)}$.

586 It is also noted that not for all predictions $\sigma_{y(Rrs)}$ can be well defined by fitting a (linear)
587 function. For example, the uncertainty from MC simulation for TChl-a varies very little
588 (0.515 – 0.54) (Figure 11A), indicating that the uncertainty is not dependent on the TChl-a
589 concentrations and does not change very much with TChl-a conditions ($R^2 = 0$). Uncertainties
590 of prokaryotic phytoplankton (prokaryotes and *Prochlorococcus*) Chl-a are not well
591 correlated to their retrievals either ($R^2 < 0.3$); here the uncertainties of their fractions are
592 highly dependent on the fraction retrievals with an inverse correlation ($R^2 > 0.77$); thus the
593 retrieval of higher fractions bears lower uncertainty. The derived regressions imply that the
594 LUTs quantify well the PFT uncertainty propagated from Rrs uncertainty for the non-
595 prokaryotic phytoplankton PFTs Chl-a and the fractions of the prokaryotic phytoplankton but
596 not for the prokaryotic Chl-a. TChl-a uncertainty is relatively stable and not related to the
597 retrieved TChl-a.

598

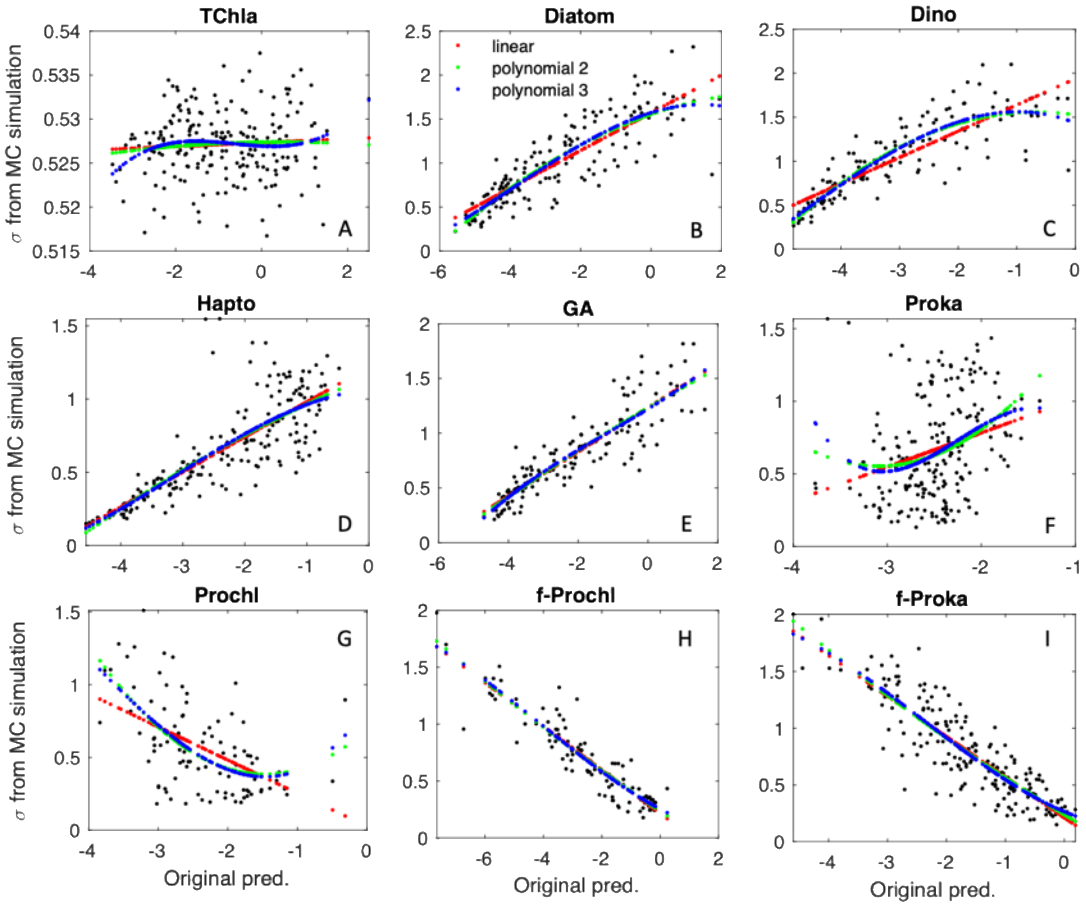

599

600 Figure 11. Scatterplots of σ_{PFT} based on the MC simulations versus originally retrieved
601 (natural-logarithmic based) PFTs. Regression lines of linear (red), polynomials with degrees
602 of 2 (green) and 3 (blue) fitting are also shown.

603 Table 6. R^2 and RMSD of the regression functions fitting the relationship between σ_{PFT} and
604 retrieved PFT quantities (using EOF-SST hybrid algorithm).

	Linear		Polynomial 2		Polynomial 3	
	R^2	RMSD	R^2	RMSD	R^2	RMSD
Diatom Chl-a	0.72	0.243	0.73	0.236	0.74	0.235
Dinoflagellates Chl-a	0.71	0.240	0.77	0.213	0.77	0.212
Green algae Chl-a	0.78	0.178	0.78	0.177	0.79	0.177
Haptophytes Chl-a	0.66	0.192	0.66	0.192	0.66	0.191
Prochlorococcus Chl-a	0.28	0.515	0.37	0.482	0.37	0.481
Prokaryotes Chl-a	0.08	0.339	0.10	0.334	0.11	0.332
TChl-a	0.00	0.004	0.01	0.004	0.03	0.004
f-*Prochlorococcus*	0.84	0.146	0.84	0.146	0.84	0.146
f-prokaryotes	0.77	0.196	0.77	0.196	0.78	0.195

3.3.2 Validation of PFT uncertainty

The linear LUTs were applied to the retrieved PFT quantities in the testing data set to determine the corresponding $\sigma_{y(Rrs)}$. The final consolidated uncertainty of the retrieved PFTs from the testing data set, σ_y, were then estimated using Eq. (5). With matchup data of the testing data set (Step 1 of Section 2.3.2), it is possible to assess whether or not the estimated uncertainties for the PFT products are accurate by comparing them to the actual error, δ_y, defined as $\delta_y = \ln(c_p) - \ln(c_o)$. If the uncertainty σ_y is truly representative of its standard deviation and thus is reliable, the distribution of the actual errors normalized by the estimated errors δ_y/σ_y should, to some extent, follow a standard centered normal distribution (Maritorena *et al.*, 2010). Therefore, to validate the estimated PFT uncertainty σ_y, the testing data set was compared to the corresponding δ_y. Note that σ_y and δ_y are both natural-logarithmic based.

Figure 12 shows the histograms of δ_y/σ_y distribution derived from the testing data set for all PFT quantities. The corresponding normal distributions determined by the mean and SD are also displayed in comparison with the centered standard normal distribution. For the majority of PFT quantities, the δ_y/σ_y distribution coincides well with the standard normal distribution, with mean values close to zero and the SD varying from 0.82 to 1.12. Relatively lower SD ($\leq$ 0.70) are found for dinoflagellates Chl-a, *Prochlorococcus* Chl-a and fraction, and the fraction converted Chl-a both for prokaryotes and *Prochlorococcus*. Nevertheless, the fraction converted prokaryotes Chl-a presents higher modeled uncertainty (i.e., lower SD of $\delta_{PFT}/\sigma_{PFT}$ in Figure 12H) compared to the direct retrieval of prokaryotes Chl-a (Figure 12F), even though the former has better prediction performance (Table 3). This suggests possible underestimation of the actual errors in the direct retrieval for prokaryotes. *Prochlorococcus* Chl-a and fraction show overall higher modeled uncertainties compared to the actual error (SD $\leq$ 0.67, Figures 12I-K). However, a skewed distribution of δ_y/σ_y is found for the direct retrieval of *Prochlorococcus* Chl-a (Figure 12I) whereas the *f-Prochlorococcus* and converted Chl-a show little skewness in their δ_y/σ_y. This suggests the modeled uncertainty is better described for the fraction and the converted *Prochlorococcus* Chl-a than the direct retrievals. The validation of the PFT uncertainty indicates that our modeled uncertainty is in general close to or higher than the actual error (SD of δ_y/σ_y is either close to or lower than 1), implying that the uncertainty assessment we performed in this study is reliable and conservative.

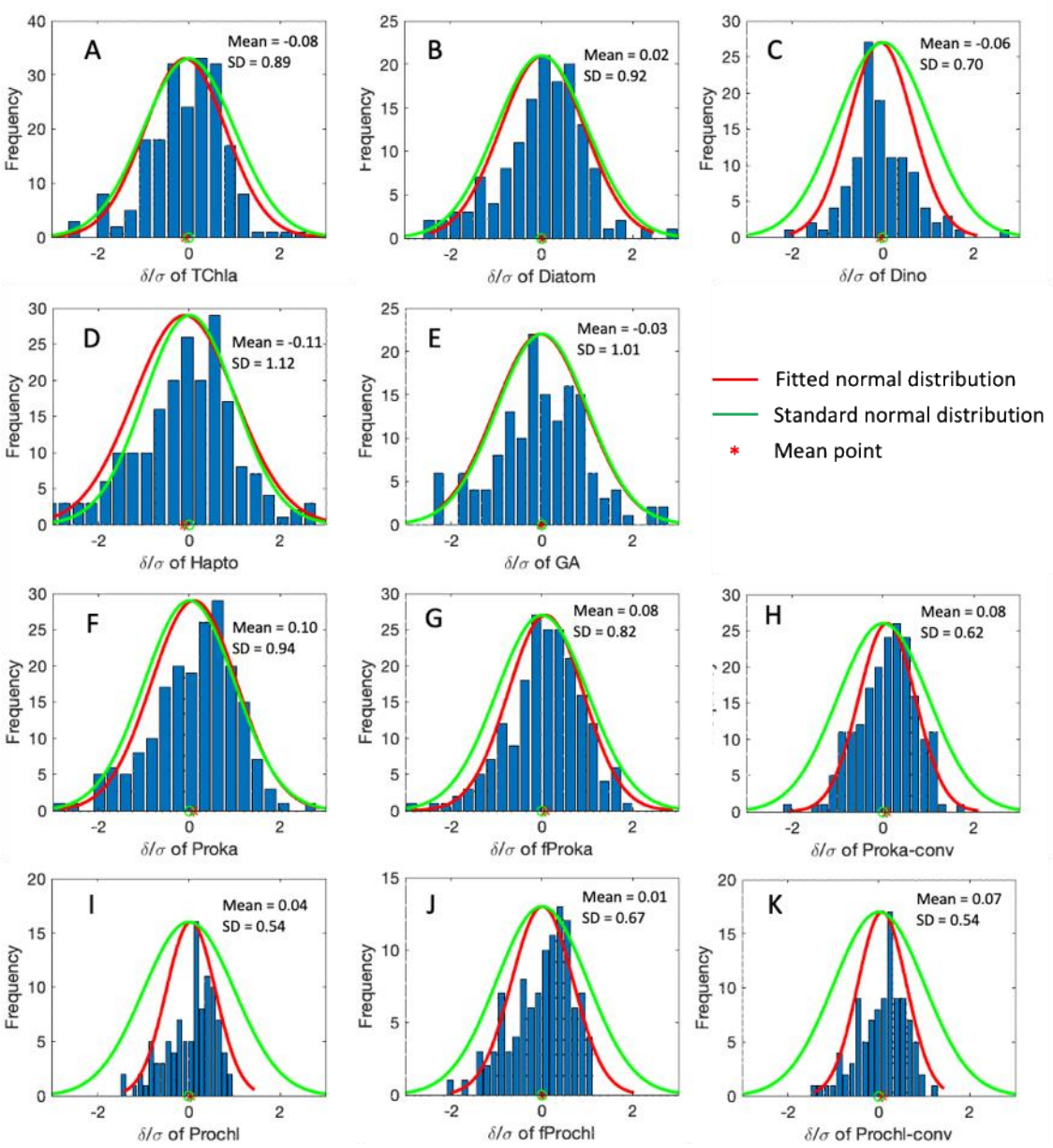

Figure 12. Distributions of the actual error normalized by the modeled propagated error ($\delta_{PFT}/\sigma_{PFT}$) for all the retrieved (using EOF-SST hybrid algorithm) PFT quantities from the testing data set: (A) TChl-a; Chl-a of (B) diatoms, (C) dinoflagellates, (D) haptophytes (E) green algae, and (F) prokaryotes; (G) *f*-prokaryotes, (H) fraction-converted prokaryotes Chl-a, (I) *Prochlorococcus* Chl-a, (J) *f-Prochlorococcus*, and (K) fraction-converted *Prochlorococcus* Chl-a. Red and green curves indicate the fitted normal distribution and the standard centered normal distribution, respectively. The red asterisk presents the mean point of the fitted distribution, and the green circle highlights the point of zero. Mean value and standard deviation (SD) of δ_y/σ_y are also shown.

3.3.3 Per-pixel PFT uncertainty

Satellite PFT uncertainties were generated for each pixel by applying all uncertainty terms in Eq. (7) to the monthly retrieved PFT products. The annual mean uncertainty for the year of 2011 was determined to be consistent with the global PFT maps in Figures 8-10. As a composite product, the annual mean uncertainty was obtained by computing the root mean square of the monthly uncertainty product, the same as for the composite uncertainty of other ocean color products, e.g., the ESA Ocean-Colour Climate Change Initiative (OC-CCI) TChl-a product (Sathyendranath *et al.*, 2019). It should be noted that in ideal case we should apply the uncertainty quantification scheme firstly to the PFT daily products, and then compute the monthly or yearly composite based on the multi-day uncertainties. However, detailed computations have shown that the monthly composites from the daily products have poorer spatial coverage compared to the directly derived monthly products. This is mainly due to less valid pixels for the nine-band Rrs spectra in the daily to monthly composites than that from the direct monthly products. In addition, the uncertainty derived directly from the monthly products is very comparable to the monthly composite generated based on daily uncertainty (e.g., for TChl-a uncertainty the R^2 = 0.98 and slope = 1.00 between the two derivations, details not shown). Therefore, in the present study we applied the uncertainty quantification scheme directly to the monthly PFT products to 1) save computing time and 2) have better spatial coverage for the derived per-pixel uncertainties.

Figure 13 demonstrates the annual composite of uncertainties for all the PFT quantities, including also the uncertainty for TChl-a derived from our EOF-SST hybrid algorithm in comparison to the uncertainty of the OC-CCI TChl-a product (Figure 13A versus 13D). Uncertainties for diatoms (Figure 13B), dinoflagellates (Figure 13C), haptophytes (Figure 13E), and green algae (Figure 13F) display similar distribution pattern with their Chl-a concentration retrievals, with low uncertainties in the gyres, and high in the high latitudes and marginal seas. The overall lowest uncertainty is obtained for haptophytes Chl-a (the natural logarithmic uncertainty varied from 0.23 to 1.26). It is also low for green algae (0.40 – 1.33), whereas diatoms Chl-a show higher uncertainty (0.53-1.73) and dinoflagellates overall the highest (0.78 – 1.70). Regarding the two prokaryotic phytoplankton, the uncertainty for the direct retrieval of prokaryotes Chl-a shows lower uncertainty in the polar regions but higher in the low latitudes (Figure 13G); that for *Prochlorococcus* shows in general high uncertainty in latitudes higher than 40° both south and north and also the gyres (Figure 13J). The uncertainties for the fractions (Figures 13H and 13K) show reverse distributions to the

fraction retrievals with low uncertainty in mid- to low latitudes compared to that in the high latitudes; the uncertainty for *f*-prokaryotes is lower than *f-Prochlorococcus* uncertainty. Fraction converted prokaryotes and *Prochlorococcus* Chl-a uncertainties basically follow the patterns of their corresponding fraction uncertainties but are higher (Figures 13I and 13L), because they are derived by combining both the fraction and TChl-a uncertainties, while the latter show little spatial variations (Figure 13A).

As the PFT prediction models are based on the multiple linear regressions, the uncertainty of the model coefficients and SST are propagated linearly to the PFT retrievals using Eq. (8). Their corresponding uncertainties are found to have much less spatial variability compared to $\sigma_{y(Rrs)}$, resulting in that the distribution patterns of the pixel-wise uncertainties generated for the PFT quantities are very much subject to $\sigma_{y(Rrs)}$ derived from the linear LUT functions. It should be noted that the LUTs built for prokaryotes and *Prochlorococcus* Chl-a can not represent their uncertainties sufficiently (Figures 11F and 11G), hence their uncertainty products (Figures 13G and 13J) should be used with caution. The uncertainties for the fractions and the converted prokaryotes and *Prochlorococcus* Chl-a, however, are reported with higher confidence as they are well described by the LUTs and the error propagation analysis. Uncertainties for the other PFT quantities are in general well and conservatively quantified, which are also justified by the uncertainty validation. Yet uncertainties for satellite derived PFTs have been rarely reported, except that Brewin, Ciavatta, *et al.* (2017) performed uncertainty evaluation on phytoplankton size classes and two phytoplankton groups (diatoms and dinoflagellates) retrieved by the re-tuned abundance/ecological based algorithm in the North Atlantic region. Though the exact values of the uncertainty estimates are not provided by Brewin, Ciavatta, *et al.* (2017), it is seen that their uncertainty maps for diatoms and dinoflagellates are within the same order of magnitudes (when converted from the base-10 logarithm to the natural-logarithm) and show similar distribution patterns with our uncertainty products in the North Atlantic Ocean.

Compared to the reported uncertainty for the TChla OC-CCI product, the uncertainty of TChl-a from our EOF-SST hybrid algorithm shows much lower uncertainty. Our TChl-a uncertainty varies from 0.53 to 0.58 (Figure 13A), presenting very little spatial variability with only slightly higher uncertainty in the gyres and some marginal seas. The OCCCI chlorophyll uncertainty ranged between 0.43 and 1.18 (Figure 13D), showing large spatial variability with much higher uncertainty in the marginal seas and high latitudes compared to our TChl-a uncertainty. Low uncertainty in and surrounding the gyres is comparable with our

uncertainty estimates. Remarkably reduced uncertainty of the TChl-a derived by our algorithm in high latitudes (> 40°) indicates that the EOF-SST hybrid algorithm has great potential in improving TChl-a estimation especially in polar regions where the standard OC algorithms always introduce high errors (IOCCG, 2015). The overall lower uncertainty in our TChl-a product also reveals at a certain scale that our estimates for most of the PFT quantities and the corresponding uncertainties are reliable.

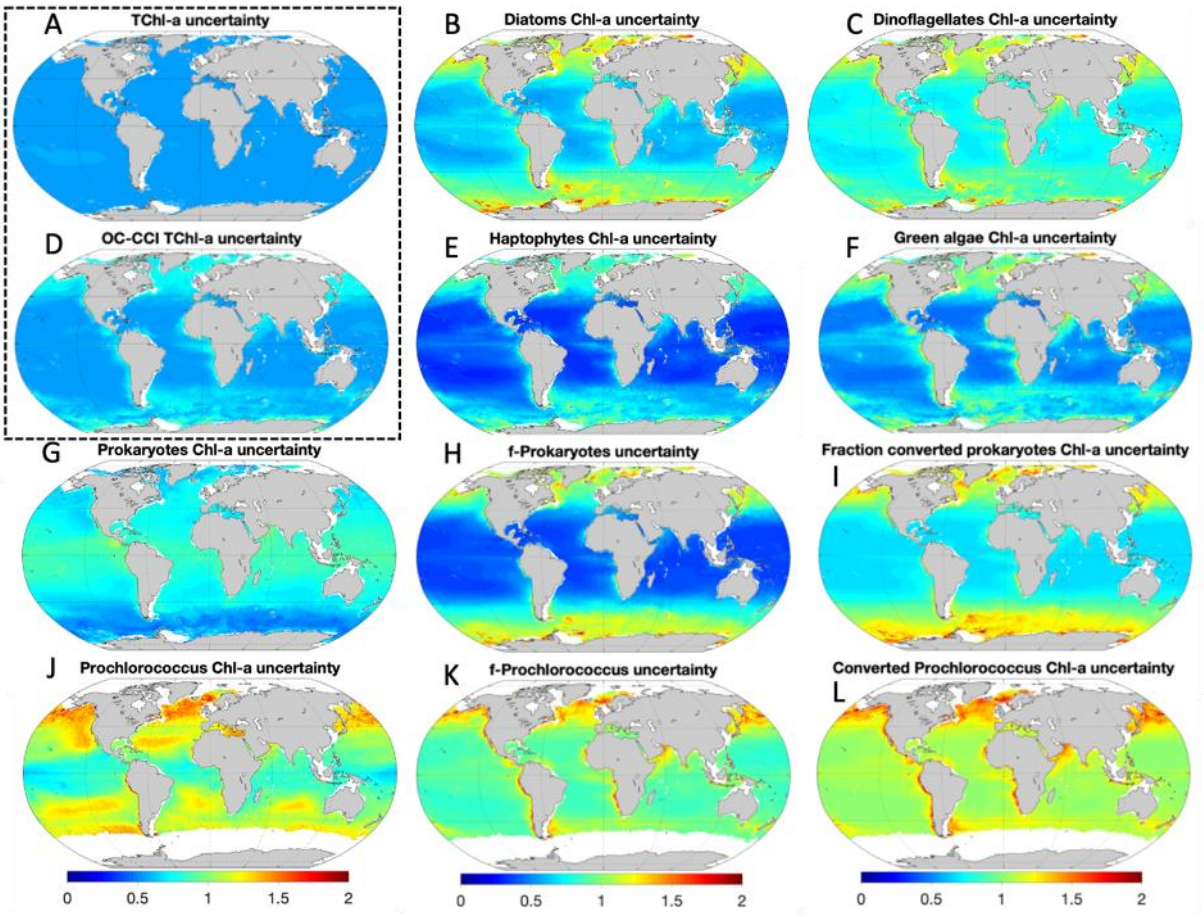

Figure 13. Per-pixel uncertainty (in natural logarithmic scale) of the annual mean of 2011 for the satellite derived PFT quantities from EOF-SST hybrid algorithm. The dashed-line box frames in particular (A) the uncertainty of TChl-a from the EOF-SST hybrid algorithm in comparison to (D) the OC-CCI TChl-a uncertainty.

4 Summary

This study improved the previously established EOF-based approach by Xi *et al.* (2020) for estimating globally the Chl-a of six PFTs using merged ocean color Rrs products. The modified retrieval scheme, named EOF-SST hybrid algorithm, was developed by using updated input data sets and accounting for the influence of SST on different PFT quantities.

Furthermore, fractions of prokaryotes and *Prochlorococcus* were also included as retrieved PFT quantities, which lead to more accurate retrievals compared to their Chl-a retrievals. The fraction retrievals were also used together with TChl-a retrievals to obtain a fraction-converted Chl-a for the two PFTs. The latter shows prominent improvements for prokaryotes Chl-a, but not for *Prochlorococcus* Chl-a. By further splitting the input data set according to the PFT dependence on SST in different SST regimes, separated retrieval algorithms for low and high temperature waters were established, presenting even much more improved performance for all PFTs than the hybrid algorithm based on the whole data set. Improvements for PFT retrievals were mostly obtained in the high latitudes. Finally, the pixel-by-pixel uncertainty of the satellite PFT retrievals was assessed by accounting for the uncertainties from input data and model parameters via an error propagation method. These satellite PFT uncertainties, for the first time reported on global scale and for spectral-based PFT retrieval approaches, provide reliable error estimates for the PFT products which allow us to better understand the product quality both in time and space.

This study uses the GlobColour merged OC products that span a period from 2002 to 2012 only. However, our EOF-SST hybrid algorithm including pixelwise uncertainties can easily be expanded to other OC sensors, such as MODIS-VIIRS merged and OLCI products. Uncertainty assessment for the PFT estimates from different satellite products, is needed for consistent long-term PFT data set from multiple satellites with assured continuity. Such a data set is required to enable tracking the shifting in phytoplankton community structure under the changing climate for example. PFT products with uncertainty estimates are also beneficial to applications of ecosystem modelling by helping to simulate and/or evaluate the model outputs, as well as being assimilated within these models to further improve forecasting marine biogeochemistry, as used by many marine services.

Acknowledgement

This work is supported by a collaborative project, OLCI-PFT (ACRI-AWI Offer #209-180104), between ACRI-ST and Phytooptics team at Alfred Wegener Institute. The contribution by S.L. was partially funded by the Deutsche Forschungsgemeinschaft (DFG, German Research Foundation)—Project number 268020496—TRR 172, within the Transregional Collaborative Research Center ArctiC Amplication: Climate Relevant Atmospheric and SurfaCe Processes, and Feedback Mechanisms (AC)3 (Project C03), and was also partly made in the framework of the state assignment of the Federal Agency for Scientific Organizations (FASO) Russia (theme 0149-2019-0015). We thank Marc Taylor for

the primary R script on the EOF method, Sonja Wiegmann for her dedication in measuring and processing the HPLC data for our own cruises, and all the previous and current Phytooptics team members who participated in the past cruises for data collection and analysis. We are thankful to all the scientists and crew involved in the global HPLC data collection and analyses for providing their pigment data. Thanks also to NASA, ESA and EUMETSAT for the SeaWiFS, MODIS, and MERIS data, and specially the GlobColour program for providing the merged ocean color L3 products. GlobColour data (http://globcolour.info) used in this study has been developed, validated, and distributed by ACRI-ST, France. This study has been conducted using E.U. Copernicus Marine Service Information in terms of CMEMS sea surface temperature products. We also thank the Ocean-Colour Climate Change Initiative (OC-CCI) program for providing global chlorophyll-a data products.

Data availability

The DPA derived PFT Chl-a for diatoms, haptophytes and prokaryotes from the pigment database I were published already in Losa *et al.* (2017) and are available from PANGAEA: https://doi.pangaea.de/10.1594/PANGAEA.875879 (Soppa *et al.*, 2017). All matchup data used in this study, including the collocated *in situ* data, nine-band Rrs data from the GlobColour merged products, and SST data, are also to be prepared and submitted to PANGAEA by end of January 2021.

References

ACRI-ST GlobColour Team, Mangin, A., & Hembise Fanton d'Andon, O. (2017). *GlobColour Product User Guide* (GC-UM-ACR-PUG-01, Version 4.1). Sophia-Antipolis: ACRI-ST.

Aiken, J., Pradhan, Y., Barlowd, R., Lavender, S., Poulton, A., Patrick, H., & Hardman-Mountford, N. (2009). Phytoplankton pigments and functional types in the Atlantic Ocean: A decadal assessment, 1995–2005. *Deep Sea Res., Part II, 56*(15), 899–917. https://doi.org/10.1016/j.dsr2.2008.09.017

Alvain, S., Moulin, C., Dandonneau, Y., & Bréon, F. M. (2005). Remote sensing of phytoplankton groups in case 1 waters from global SeaWiFS imagery. *Deep Sea Res., Part I, 52*(11), 1989–2004. https://doi.org/10.1016/j.dsr.2005.06.015

Alvain, S., Moulin, C., Dandonneau, Y., & Loisel, H. (2008). Seasonal distribution and succession of dominant phytoplankton groups in the global ocean: A satellite view. *Global Biogeochem. Cycles, 22*(3), GB3001, https://doi.org/10.1029/2007GB003154

Amante, C., & Eakins, B.W. (2009). *ETOPO1 1 Arc-Minute Global Relief Model: Procedures, Data Sources and Analysis* (NOAA Technical Memorandum NESDIS NGDC-24). Boulder, CO: National Geophysical Data Center.

Antoine, D., d'Ortenzio, F., Hooker, S. B., Bécu, G., Gentili, B., Tailliez, D., & Scott, A. J. (2008). Assessment of uncertainty in the ocean reflectance determined by three satellite ocean color sensors (MERIS, SeaWiFS and MODIS-A) at an offshore site in the Mediterranean Sea

(BOUSSOLE project). *J Geophys. Res. Ocean., 113*, C07013. https://doi.org/10.1029/2007JC004472

Bracher, A., Xi, H., Dinter, T., Mangin, A., Strass, V. H., von Appen, W.-J., & Wiegmann, S. (2020). High resolution water column phytoplankton composition across the Atlantic Ocean from ship-towed vertical undulating radiometry. *Front. Mar. Sci., 7*, 235, https://doi.org/10.3389/fmars.2020.00235

Bracher, A., Bouman, H. A., Brewin, R. J. W., Bricaud, A., Brotas, V., Ciotti, A. M., et al. (2017). Obtaining Phytoplankton Diversity from Ocean Color: A Scientific Roadmap for Future Development. *Front. Mar. Sci., 4*, 1–15. https://doi.org/10.3389/fmars.2017.00055

Bracher, A., Taylor, M.H., Taylor, B., Dinter, T., Röttgers, R., & Steinmetz, F. (2015). Using empirical orthogonal functions derived from remote-sensing reflectance for the prediction of phytoplankton pigment concentrations. *Ocean Sci., 11*, 139-158. https://doi.org/10.5194/os-11-139-2015

Bracher, A., Vountas, M., Dinter, T., Burrows, J. P., Röttgers, R., & Peeken, I. (2009). Quantitative observation of cyanobacteria and diatoms from space using PhytoDOAS on SCIAMACHY data. *Biogeosciences, 6*, 751-764. https://doi.org/10.5194/bg-6-751-2009

Brewin, R. J. W., Ciavatta, S., Sathyendranath, S., Jackson, T., Tilstone, G., Curran, K., et al. (2017). Uncertainty in Ocean-Color Estimates of Chlorophyll for Phytoplankton Groups. *Front. Mar. Sci., 4*, 104. https://doi.org/10.3389/fmars.2017.00104

Brewin, R. J. W., Tilstone, G., Jackson, T., Cain, T., Miller, P., Lange, P. K., et al. (2017). Modelling size-fractionated primary production in the Atlantic Ocean from remote sensing. *Prog. Oceanogr., 158*, 130-149. https://doi.org/10.1016/j.pocean.2017.02.002

Brewin, R. J. W., Sathyendranath, S., Hirata, T., Lavender, S. J., Barciela, R. M., & Hardman-Mountford, N. J. (2010). A three-component model of phytoplankton size class for the Atlantic Ocean. *Ecol. Modell., 221*(11), 1472-1483. https://doi.org/10.1016/j.ecolmodel.2010.02.014

Brewin, R. J. W., Sathyendranath, S., Jackson, T., Barlow, R., Brotas, V., Airs, R., & Lamont, T. (2015). Influence of light in the mixed-layer on the parameters of a three-component model of phytoplankton size class. *Remote Sens. Environ., 168*, 437-450. https://doi.org/10.1016/j.rse.2015.07.004

Brotas, V., Brewin, R. J. W., Sá, C., Brito, A. C., Silva, A., Mendes, C. R., et al. (2013). Deriving phytoplankton size classes fromsatellite data: validation along a trophic gradient in the eastern Atlantic Ocean. *Remote Sens. Environ., 134*, 66–77. https://doi.org/10.1016/j.rse.2013.02.013

Ciotti, A. M., & Bricaud, A. (2006). Retrievals of a size parameter for phytoplankton and spectral light absorption by colored detrital matter from water-leaving radiances at SeaWiFS channels in a continental shelf region off Brazil. *Limnol. Oceanogr. Methods, 4*, 237–253. https://doi.org/10.4319/lom.2006.4.237

Claustre, H., Hooker, S. B., Van Heukelem, L., Berthon, J.-F., Barlow, R., Ras, J., et al. (2004). An intercomparison of HPLC phytoplankton pigment methods using in situ samples: Application to remote sensing and database activities. *Mar. Chem., 85*(1-2), 41–61. https://doi.org/10.1016/j.marchem.2003.09.002

Correa-Ramirez, M., Morales, C. E., Letelier, R., Anabalon, V., & Hormazabal, S. (2018). Improving the remote sensing of phytoplankton functional types (PFT) using empirical orthogonal functions: a case study in a coastal upwelling region. *Remote Sens., 10*(4), 498. https://doi.org/10.3390/rs10040498

Craig, S. E., Jones, C. T., Li, W. K. W., Lazin, G., Horne, E., Caverhill, C., & Cullen, J. J. (2012). Deriving optical metrics of coastal phytoplankton biomass from ocean colour. *Remote Sens. Environ., 119*, 72–83. https://doi.org/10.1016/j.rse.2011.12.007

de Mora, L., Butenschön, M., & Allen, J. I. (2016). The assessment of a global marine ecosystem model on the basis of emergent properties and ecosystem function: a case study with ERSEM. *Geosci. Model Dev.*, *9*, 59–76. https://doi.org/10.5194/gmd-9-59-2016

Devred, E., Sathyendranath, S., & Platt, T. (2009). Decadal changes in ecological provinces of the Northwest Atlantic Ocean revealed by satellite observation. *Geophys. Res. Letter.*, *36*, L19607. https://doi.org/10.1029/2009GL039896

Devred, E., Sathyendranath, S., Stuart, V., Maass, H., Ulloa, O., & Platt, T. (2006). A two-component model of phytoplankton absorption in the open ocean: Theory and applications. J. *Geophys. Res. Ocean.*, *111*, C03011, https://doi.org/10.1029/2005JC002880

Donlon, C. J., Martin, M., Stark, J., Roberts-Jones, J., Fiedler, E., & Wimmer, W. (2012). The operational sea surface temperature and sea ice analysis (OSTIA) system. *Remote Sens. Environ.*, *116*, 140-158. https://doi.org/10.1016/j.rse.2010.10.017

Falkowski, P. G., Laws, E. A., Barber, R. T., & Murray, J. W. (2003). Phytoplankton and their role in primary, new, and export production. In M.J.R. Fasham (Eds.), *Ocean biogeochemistry. Global Change — The IGBP Series (closed)* (pp99-121). Berlin, Heidelberg: Springer. *https://doi.org/10.1007/978-3-642-55844-3_5*

Flombaum, P., Gallegos, J. L., Gordillo, R. A., Rincon, J., Zabala, L. L., Jiao, N., et al. (2013). Present and future global distributions of the marine Cyanobacteria Prochlorococcus and Synechococcus. *Proc. Natl. Acad. Sci. 110*, 9824–9829. https://doi.org/10.1073/pnas.1307701110

Hirata, T., Hardman-Mountford, N. J., Brewin, R. J. W., Aiken, J., Barlow, R., Suzuki, K., et al. (2011). Synoptic relationships between surface Chlorophyll-a and diagnostic pigments specific to phytoplankton functional types. *Biogeosciences, 8*, 311–327. https://doi.org/10.5194/bg-8-311-2011

Hirata, T., Saux Picart, S., Hashioka, T., Aita-Noguchi, M., Sumata, H., Shigemitsu, M., et al. (2013). A comparison between phytoplankton community structures derived from a global 3D ecosystem model and satellite observation. *J. Mar. Syst., 109–101*, 129–137. https://doi.org/10.1016/j.jmarsys.2012.01.009

Holt, J., Allen, J. I., Anderson, T. R., Brewin, R. J. W., Butenschön, M., Harle, J., et al. (2014). Challenges in integrative approaches to modelling the marine ecosystems of the North Atlantic: physics to fish and coasts to ocean. *Prog. Oceanogr., 129*, 285–313. https://doi.org/10.1016/j.pocean.2014.04.024

IOCCG (2014). Phytoplankton functional types from space. In S. Sathyendranath and V. Stuart (Eds.) *Reports of the International Ocean Color Coordinating Group* (No. 15). Dartmouth, NS: IOCCG.

IOCCG (2015). Ocean Colour Remote Sensing in Polar Seas. In M. Babin, K. Arrigo, S. Bélanger, M.-H. Forget (Eds.) *Reports of the International Ocean Color Coordinating Group* (No. 16). Dartmouth, NS: IOCCG.

IOCCG (2019). Uncertainties in ocean colour remote sensing. In F. Melin (Eds.) *Reports of the International Ocean Color Coordinating Group* (No. 18). Dartmouth, NS: IOCCG.

JCGM (2008). *Evaluation of Measurement Data - Guide to the Expression of Uncertainty in Measurement*. JCGM 100:2008.

Kostadinov, T. S., Milutinović, S., Marinov, I., & Cabré, A. (2016). Carbon-based phytoplankton size classes retrieved via ocean color estimates of the particle size distribution. *Ocean Sci., 12*, 561–575. https://doi.org/10.5194/os-12-561-2016

Kostadinov, T. S., Siegel, D. A., & Maritorena, S. (2009). Retrieval of the particle size distribution from satellite ocean color observations. *J. Geophys. Res. Ocean., 114*, 09015. https://doi.org/10.1029/2009JC005303

Lange P. K., Werdell P. J., Erickson Z. K., Dall'Olmo G., Brewin R., Zubkov M., et al. (2020). Radiometric approach for the detection of picophytoplankton assemblages across oceanic fronts. *Optics Express., 28*(18), 25682-25705. https://doi.org/10.1364/OE.398127

Le Quéré, C., Harrison, S. P., Prentice, C. I., Buitenhuis, E. T., Aumonts, O., Bopp L., et al. (2005). Ecosystem dynamics based on plankton functional types for global ocean biogeochemistry models. *Global Change Biology, 11*, 2016-2040. https://doi.org/10.1111/j.1365-2486.2005.1004.x

Lee, Z., Arnone, R., Hu, C., Werdell, P. J., & Lubac, B. (2010). Uncertainties of optical parameters and their propagations in an analytical ocean color inversion algorithm. *Appl. Optics, 49*, 369–381. https://doi.org/10.1364/AO.49.000369

Losa, S. N., Soppa, M. A., Dinter, T., Wolanin, A., Brewin, R.J.W., Bricaud, A., et al. (2017). Synergistic Exploitation of Hyper- and Multi-Spectral Precursor Sentinel Measurements to Determine Phytoplankton Functional Types (SynSenPFT). *Front. Mar. Sci., 4*, 1–22. https://doi.org/10.3389/fmars.2017.00203

Losa, S. N., Dutkiewicz, S., Losch, M., Oelker, J., Soppa, M. A., Trimborn, S., Xi, H., & Bracher, A. (2019). On modeling the Southern Ocean Phytoplankton Functional Types, *Biogeosciences Discuss.*, https://doi.org/10.5194/bg-2019-289

Lubac, B., & Loisel, H. (2007). Variability and classification of remote sensing reflectance spectra in the eastern English Channel and southern North Sea. *Remote Sens. Environ., 110*(1), 45-58. https://doi.org/10.1016/j.rse.2007.02.012

Maritorena, S., Hembise Fanton d'Andon, O., Mangin, A., & Siegel, D. A. (2010). Merged satellite ocean color data products using a bio-optical model: characteristics, benefits and issues. *Remote Sens. Environ. 114*, 1791–1804. https://doi.org/10.1016/j.rse.2010.04.002

McKinna, L. I. W., Cetinic, I., Chase, A. P. & Werdell, P. J. (2019). Approach for Propagating Radiometric Data Uncertainties Through NASA Ocean Color Algorithms. *Front. Earth Sci., 7*, 176. https://doi.org/10.3389/feart.2019.00176

Mélin, F., & Franz, B. A. (2014). Assessment of satellite ocean colour radiometry and derived geophysical products. In G. Zibordi, C. Donlon, A. Parr (Eds.) *Optical Radiometry for Oceans Climate Measurements*, Experimental Methods in the Physical Sciences (Vol. 47). Academic Press.

Mouw, C., Hardman-Montford, N., Alvain, S., Bracher, A., Brewin, R. J. W., Bricaud, A., et al. (2017). A Consumer's Guide to Satellite Remote Sensing of Multiple Phytoplankton Groups in the Global Ocean. *Front. Mar. Sci., 4*, 00041, https://doi.org/10.3389/fmars.2017.00041

Johnson, R., Strutton, P. G., Wright, S. W., McMinn, A., & Meiners, K. M. (2013). Three improved satellite chlorophyll algorithms for the Southern Ocean. *J. Geophy. Res. Ocean., 118*, 3694-3703. https://doi.org/10.1002/jgrc.20270

Palacz, A. P., St. John, M. A., Brewin, R. J. W., Hirata, T., & Gregg, W. W. (2013). Distribution of phytoplankton functional types in high-nitrate, low-chlorophyll waters in a new diagnostic ecological indicator model. *Biogeosciences, 10*, 7553-7574. https://doi.org/10.5194/bg-10-7553-2013

Pradhan, H. K., Völker, C., Losa, S. N., Bracher, A., & Nerger L. (2019). Assimilation of global total chlorophyll OC-CCI data and its impact on individual phytoplankton fields. *J. Geophys. Res. Ocean., 124*, 470-490. https://doi.org/10.1029/2018JC014329

Pradhan, H. K., Völker, C., Losa, S. N., Bracher, A., & Nerger, L. (2020). Global assimilation of ocean-color data of phytoplankton functional types: Impact of different datasets. *J. Geophys. Res. Ocean., 125*, e2019JC015586. https://doi.org/10.1029/2019JC015586

Qi, L., Lee, Z., Hu, C., & Wang, M. (2017). Requirement of minimal signal-to-noise ratios of ocean color sensors and uncertainties of ocean color products. *J. Geophys. Res. Ocean., 122*, 2595–2611. https://doi.org/10.1002/2016JC012558

Raitsos, D. E., Lavender, S. J., Maravelias, C. D., Haralabous, J., Richardson, A. J., & Reid, P. C. (2008). Identifying four phytoplankton functional types from space: An ecological approach. *Limnol. Oceanogr., 53*(2), 605-613. https://doi.org/10.4319/lo.2008.53.2.0605

Sathyendranath, S., Brewin, R. J. W., Brockmann, C., Brotas, V., Calton, B., Chuprin, A., et al. (2019). An ocean-colour time series for use in climate studies: the experience of the Ocean-Colour Climate Change Initiative (OC-CCI). *Sensors, 19*, 4285. https://doi.org/10.3390/s19194285

Sathyendranath, S., Jackson, T., Brockmann, C., Brotas, V., Calton, B., Chuprin, A., et al. (2020). ESA Ocean Colour Climate Change Initiative (Ocean_Colour_cci): Global chlorophyll-a data products gridded on a sinusoidal projection, Version 4.2. Centre for Environmental Data Analysis, *21 October 2020 citation*. https://catalogue.ceda.ac.uk/uuid/99348189bd33459cbd597a58c30d8d10

Soja-Woźniak, M., Craig, S. E., Kratzer, S., Wojtasiewicz, B., Darecki, M., & Jones, C. T. (2017). A Novel Statistical Approach for Ocean Colour Estimation of Inherent Optical Properties and Cyanobacteria Abundance in Optically Complex Waters. *Remote Sens., 9*, 1–22. https://doi.org/10.3390/rs9040343

Soppa, M. A., Hirata, T., Silva, B., Dinter, T., Peeken, I., Wiegmann, S., & Bracher, A. (2014). Global retrieval of diatom abundance based on phytoplankton pigments and satellite data. *Remote Sens. 6*, 10089–10106. https://doi.org/10.3390/rs61010089

Soppa, M.A., Peeken, I., & Bracher, A. (2017). Global chlorophyll "a" concentrations for diatoms, haptophytes and prokaryotes obtained with the diagnostic pigment analysis of HPLC data compiled from several databases and individual cruises. PANGAEA. https://doi.org/10.1594/PANGAEA.875879

Taylor, B. B., Taylor, M. H., Dinter, T., & Bracher, A. (2013). Estimation of relative phycoerythrin concentrations from hyperspectral underwater radiance measurements - A statistical approach. *J. Geophys. Res. Ocean. 118*, 2948–2960. https://doi.org/10.1002/jgrc.20201

Uitz, J., Claustre, H., Morel, A., & Hooker, S. B. (2006). Vertical distribution of phytoplankton communities in open ocean: An assessment based on surface chlorophyll. J. *Geophys. Res. Ocean., 111*, C08005. https://doi.org/10.1029/2005JC003207

Vidussi, F., Claustre, H., Manca, B. B., Luchetta, A., & Marty, J.-C. (2001). Phytoplankton pigment distribution in relation to upper thermocline circulation in the eastern Mediterranean Sea during winter. *J. Geophys. Res. Ocean., 106*(C9), 19,939-19,956. https://doi.org/10.1029/1999JC000308

Ward, B. A., Dutkiewicz, S., Jahn, O., & Follows, M. J. (2012). A size-structured food-web model for the global ocean. *Limnol. Oceanogr. 57*, 1877–1891. https://doi.org/10.4319/lo.2012.57.6.1877

Ward, B.A. (2015). Temperature-correlated changes in phytoplankton community structure are restricted to polar waters. *PLoS One*. https://doi.org/10.1371/journal.pone.0135581

Werdell, P. J., McKinna, L., Boss, E., Ackleson, S., Craig, S., Gregg, W., et al. (2018). An overview of approaches and challenges for retrieving marine inherent optical properties from ocean color remote sensing. *Prog. Oceanogr., 160*, 186-212. https://doi.org/10.1016/j.pocean.2018.01.001

Werdell, P. J., Roesler, C. S., & Goes, J. I. (2014). Discrimination of phytoplankton functional groups using an ocean reflectance inversion model. *Appl. Opt., 53*, 4833. https://doi.org/10.1364/ao.53.004833

Worsfold, M., Good, S., McLaren, A., Fiedler, E., Roberts-Jones, J., & Martin, M. (2014). Quality Information Document Global Ocean OSTIA Sea Surface Temperature Reprocessing SST-GLO-SST-L4-REP-OBSERVATIONS-010-011. Ref: CMEMS-SST-QUID-010-011.

Xi, H., Losa, S. N., Mangin, A., Soppa, M. A., Garnesson, P., Demaria, J., et al. (2020). Global retrieval of phytoplankton functional types based on empirical orthogonal functions using CMEMS GlobColour merged products and further extension to OLCI data. *Remote Sens. Environ., 240*, 111704. https://doi.org/10.1016/j.rse.2020.111704

Xiao, Y., & Friedrichs, M. A. M. (2014). The assimilation of satellite-derived data into a one-dimensional lower trophic level marine ecosystemmodel. *J. Geophys. Res. Ocean., 119*, 2691–2712. https://doi.org/10.1093/plankt/fbp127